Proceedings of the ASME Turbo Expo 2026: Turbomachinery Technical Conference and Exposition
GT2026
June xx-June xx, 2026, Milan, Italy

GT2026-152033X

TURBOMACHINERY SIMULATION IMPACT ON DESIGN, UNDERSTANDING, AND OPTIMIZATION (EXTENDED)

Mark G. Turner
Senior Technologist, Aeropropulsion
Propulsion Division, Research and Engineering Directorate
NASA Glenn Research Center
21000 Brookpark Rd, MS 5-3
Cleveland, OH 44135
mark.turner@uc.edu

ABSTRACT

This paper presents the impact of Turbomachinery Simulation from simple analytical simulations to high fidelity CFD and Finite Element Analyses on the design of turbomachinery and the understanding of flow physics that is then used to improve design approaches. The impact of optimization is also presented. The best approach for tool development is to work with a compressor, fan, or turbine designer or to work on the design process directly. The paper represents the work and impact of the author over his 45-year career and provides insight for both new and experienced engineers. The paper explores applications of distortion from a downstream fan frame, the first uses of 3D CFD for fan, compressor and turbine design, and for the simulation of the GE90 turbofan engine in 3D.

The positive impact in performance due to turbomachinery simulation has led to much improved turbomachinery efficiencies and reduced fuel burn of engines and aircraft. This benefit has been due to the direct interaction with the designers, so the simulations impact the design and product. The added impact of multi-disciplinary simulations has also had impact on greater life, less weight, and reduced noise. Future direction for simulations are also presented.

1 To the Reviewers

I have not felt well for the past year while I have written this extension to the 2024 paper. Because of this, it is not as expansive as I would like. I am feeling better and should have a complete paper before re-reviews are done. I have included section and subsection titles that I expect to work on for the final paper and will be part of the lecture.

NOMENCLATURE

this section is not complete and some variables are for the future sections.

A	Averaging Operator
AF	Amplification Factor
ATNA	Advanced Turbine Nozzle Aerodynamic
C	Curvature
C_p	Specific Heat at Constant Pressure
DF	Diffusion Factor
H_s	Shape Factor
LAR	Low Aspect Ratio
M	Mach number
$\mathbf{N_2d}$	Axisymmetric Navier-Stokes Operator (in 2D)
$\mathbf{N_3d}$	Navier-Stokes Operator in 3D
P	Prolongation or Injection Operator
P_T or PT	Total Pressure

PR	Total Pressure Ratio
T_T or TT	Total Temperature
TR	Total Temperature Ratio
U	wheel speed = ωr
V	velocity (also Volume)
VE	Viscous Euler
$WR4$	Wennerstrom Rotor 4 test case
Greek	
δ	Boundary layer thickness
δ^*	Boundary Layer Displacement Thickness
η_c	Compressor Adiabatic Efficiency
θ	Tangential direction or Boundary Layer Momentum Thicl
λ	Blockage Coefficient
σ	stress
ϕ	Flow Coefficient and radial angle of flow
ψ	Loading Coefficient
ω	angular speed of rotation
$\bar{\omega}$	Compressor Loss Coefficient
Subscripts	
1	leading edge plane
c	corrected
m	meridional
r	rig
STP	Standard Temperature and Pressure

2 INTRODUCTION

Turbomachinery has evolved tremendously during the past 45 years that I have been an engineer/researcher. This paper is written to explain the work I have done and describe the insights I have gained personally by the simulations of turbomachinery that have influenced designs, gained understanding, and enabled optimization. It is not intended as a review of all existing benefits of turbomachinery simulations, but to expound on areas I have worked on directly. Most of the information has been published before, but often in little known references. This paper allows the important concepts to be seen by a wider audience. It is also useful to consider the work as a collection with the common theme of the design implications.

The work presented reflects the 20 years experience with GE Aircraft Engines (now GE Aerospace), nearly 20 years as a professor of Aerospace Engineering at the University of Cincinnati, and the 4 years at NASA where I am currently a Senior Technologist in Aeropropulsion. This time has been exciting for simulations as computers have increased in speed and memory and computational algorithms have advanced for solving increasingly complex physics. This has allowed for more routine and reliable simulations with greater fidelity and the ability to be used in optimization.

An image of the author in front of a GE90 94B is shown in Figure 1 [1]. Two of the codes the author worked on while at GE (AEGIS and a 3D Navier-Stokes Solver) were used to improve the design of this engine. It is by working closely with the aerodynamic designers and creating software that was logically integrated into the design system that enabled the use of advanced simulations to impact the designs.

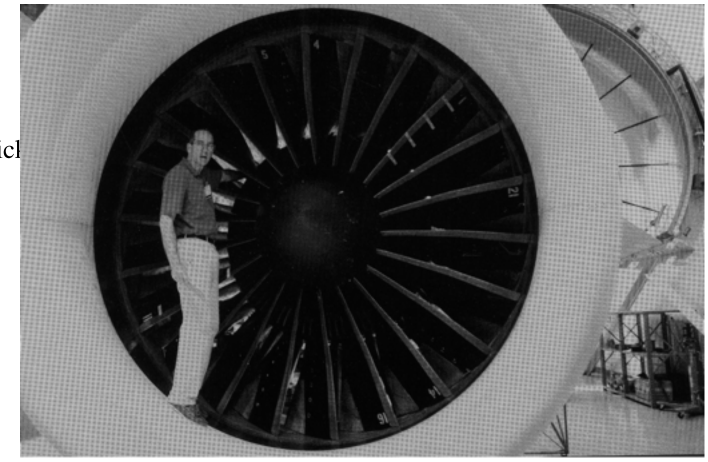

FIGURE 1: A picture of the author in 1997 in the inlet of a GE90-94B [1] . It has a fan diameter of 3.05 m (120 in). Need permission to state author's contribution to Viscous Euler contributed to 3D design of GE90 fan and AEGIS was used for the OGV.

3 Organization of Paper

This paper is arranged mostly chronologically which is also related to the fidelity of simulations. The paper starts with 2D or quasi-3D simulations with multiple airfoils to understand and design for distortion from downstream potential effects. Following that is 3D Reynolds Averaged Navier-Stokes simulations for isolated blade rows and examples of how these codes were utilized in design. Following this is the application and extensions of the Average Passage formulation, several applications, and physical insights. Optimization application and approaches are discussed next. With fast computers and parametric design definition, optimization allows for creating improved designs without extensive empiricism. In addition to the technical work, I have offered career advice to many students and early career engineers. I have included a section on Words of Wisdom and Advice that should be useful. Following this is a look to the future and a set of conclusions.

4 CFD Verification

Computational Fluid Dynamics is extremely useful in design, although there are limitations. John Denton had a very good paper on the limitations of CFD in Turbomachinery [2], although some of those limitations have been reduced in the 15 years since that paper was written, with new algorithms, faster and larger computers, and improved flow physics modeling. However, there is always need for verification of the simulation to ensure there is meaningful value in the results.

4.1 Checklist

Some CFD solutions are desired to get an idea of where the flow is going. For turbomachinery, you want to understand performance. In either case, one should have a checklist that is used to ensure a simulation is useful for its intended application. The grid resolution, the fidelity of the simulation (steady, time accurate, or LES) also depends on how the simulation will be used.

- If it is for a relative performance difference, a medium grid can be used.
- If it is for an absolute performance difference, a fine grid should be used:
  - $*$ y^+ values will need to be checked after solution is run
  - $*$ If wall functions are used, y^+ should be between 25 and 100
  - $*$ If wall functions are not used and adiabatic, the $y^+ < 1$
- Is it converged?
  - $*$ Have residuals dropped by at least 3 orders of magnitude.
  - $*$ $0.995 < \frac{Massflowatinlet}{massflowatexit} < 1.005$. Less change may be required if performance difference is small.
- Has it diverged?
  - $*$ Boundary Conditions set right?
  - $*$ Omega right sign?
  - $*$ Lower CFL
  - $*$ Run for 10 iterations to check BCs
  - $*$ Run for 10 iterations less than when if blows up and check where problem might be
- Has it hit a limit cycle? Is it neither converged or diverged?

5 Distortion from Downstream

Often when discussing distortion, it is the distorted flow from upstream due to cross flow into an inlet or non-uniform boundary layers. However, the distortion from downstream due to blockage of large struts and pylons creates a back-pressuring effect on the flow upstream due to the tangentially non-uniform potential field. This distortion from downstream can cause performance and aeromechanical issues if unmitigated. By understanding the flowfield and taking appropriate design steps, the distortion seen by the upstream rotor can be reduced. The AEGIS, AErodynamic General Implict Solver, [3] was written by the author to solve for multiple bodies in 2D, including the full annulus simulation of fan frames. It has been used for the design of fan frames and understanding of back-pressuring effects, and is still available in the suite of software tools available to the GE aerodynamic designer.

5.1 Fan OGVs with Pylon

In the late 1970s and early 1980s, NASA created the Energy Efficient Engine (EEE) program to improve the performance and efficiency of jet engines. A book by M.D. Bowles [4] describes this program and its huge impact. GE was one of the companies that participated. I find the EEE reports by NASA and each of the engine companies to be amazing references for understanding components and systems. The goals of that program and the component designs are still relevant even though there have been continued major improvements by using advanced computational tools and new materials. The GE EEE program developed an entirely new centerline turbofan engine. The GE EEE fan [5] had non-uniform OGV blades. It had been designed with a somewhat crude aerodynamic approach. Figure 2 shows the full annulus EEE fan geometry at midspan unwrapped. The upper pylon is needed for structural reasons as well as to serve as routing for fuel to the engine and bleed air to the aircraft. It creates a very large back pressuring effect on the OGVs and upstream fan rotor blades.

AEGIS is very accurate even with course grids due to the details of the algorithm that are described by Turner and Keith [3]. Two designs of the GE EEE fan frame were analyzed. One with the as-tested multi-vane design which had blades that guided the flow smoothly around the pylon. The other design had all the vanes the same around the annulus. This is shown in Figure 3. The Mach contours calculated for the multi-vane design are shown near the pylon leading edge in Figure 4, and the streamlines are shown in Figure 5. At an axial location midway between the OGV trailing edge and large pylon leading edge (see Figure 4), the flow angle in the tangential direction is plotted in Figure 6 for the uniform and multi-vane designs as a function of circumferential angle. The static pressure is compared in a similar manner in Figure 7. Figure 6 shows about -10 to +8 degree variation for the multi-vane design and -5 to +5 degrees for the uniform-vane design. This produces a corresponding static pressure variation around the annulus that is reduced for the multi-vane design which has accomplished its goal of reducing the distortion from the large pylon. Another feature of AEGIS is that the upstream boundary conditions of total pressure and total temperature can utilize a rotor characteristic as shown in Figure 8. The actual flow physics is unsteady in the rotor relative frame as the rotor will see a variation in exit static pressure as a function of time. AEGIS uses the rotor characteristic as a quasi-steady model. At the upstream boundary, the meridional velocity, V_m, varies due to the distortion from downstream. The flow coefficient, $\phi = \frac{V_m}{U}$ then varies and the effective variation of ϕ is shown for both the uniform vane and multi-vane designs. The variation in total pressure from this simulation and utilizing the rotor characteristic is shown in Figure 9 and compared to the experimental results from the fan rig test [5]. The comparison is made at the axial location just downstream of the OGV trailing edge for which there were 5 radial rakes spaces as shown circumferentially. The radius of the simulation was between two radial rake locations so two radii from the rakes are shown. The circumferential position is periodic so 90 degrees on either side are repeated to better appreciate the variation. It can be seen that there is resonable agreement with the simulation of the multi-vane design which was the one tested. This is an excellent result considering the many assumptions made: 2D, inviscid, and quasi-steady rotor characteristic.

All large turbofan engines and even some smaller ones have different types of OGV vanes around the annulus with different stagger and/or camber. They are usually manufactured with several vanes as a group and made so they can only fit in the correct place around the annulus.

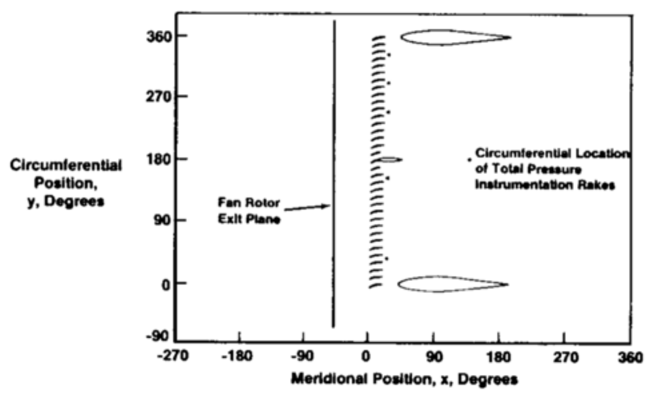

FIGURE 2: GE EEE fan frame geometry at midspan unwrapped around the annulus showing the OGVs, upper pylon (duplicated at top and bottom), and lower strut [3].

5.2 Vane-Strut Interaction

Another application of AEGIS was used to explore a compressor rotor blade forced response due to a downstream vane-strut potential interaction [6]. The rotor, stator and strut geometry are shown in Figure 10. The paper [6] derives an actuator disk analysis about how a circumferential pressure variation will amplify going upstream due to the static pressure being lower at the leading edge than the trailing edge. A schematic of the jump across the vane is shown in the top of Figure 11 while the bottom has the Amplification Factor, AF, plotted as a function of leading edge Mach number, M_1 and leading edge flow angle. The

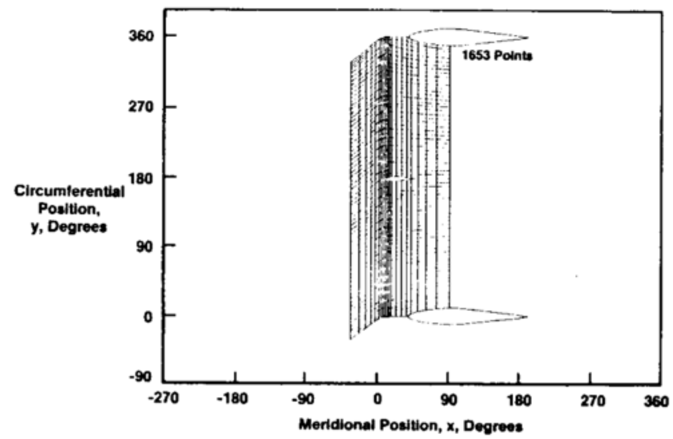

FIGURE 3: The AEGIS grid of the GE EEE fan frame at midspan that includes the OGVs, upper pylon (duplicated at top and bottom), and lower strut [3].

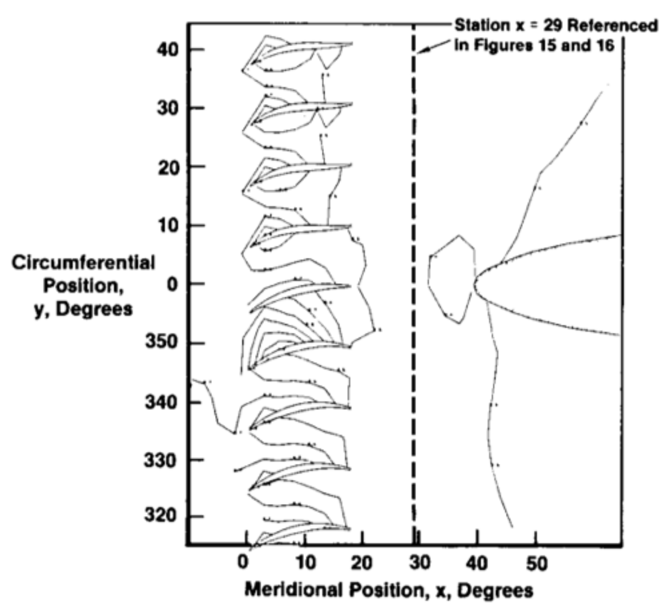

FIGURE 4: Mach contours from the AEGIS solution of the multi-vane design in the vicinity of the upper pylon. [3].

Amplification Factor is defined as

$$AF = \frac{\delta P_1}{\delta P_2} \tag{1}$$

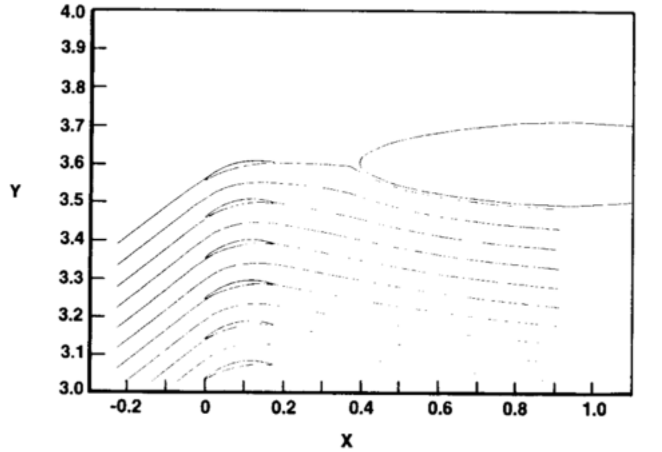

FIGURE 5: Computed streamlines from the AEGIS solution of the multi-vane design around the upper pylon [3].

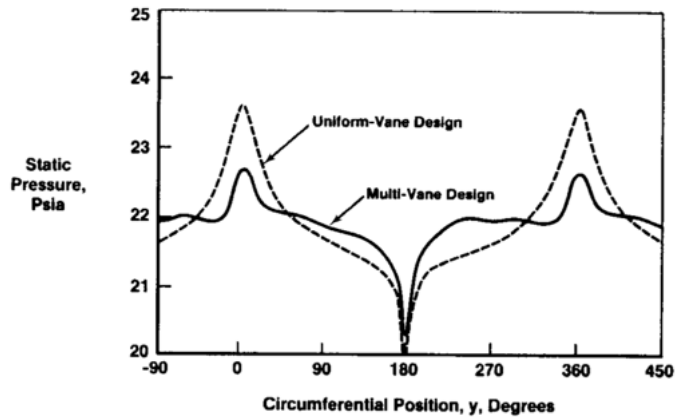

FIGURE 7: Static pressure around the annulus comparing the uniform vane and multi-vane designs at an axial location midway between the OGV trailing edge and large pylon leading edge [3].

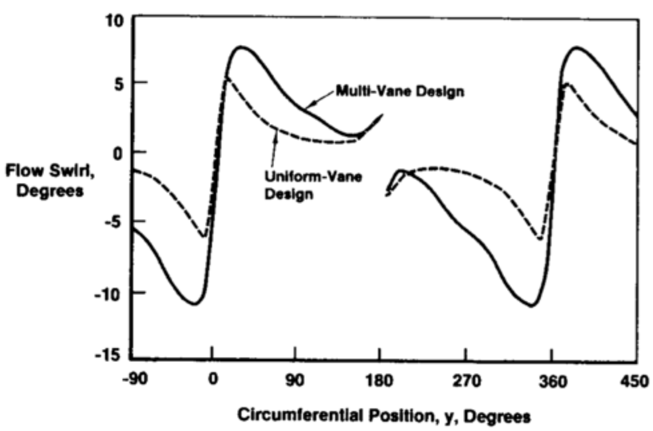

FIGURE 6: Flow swirl (angle in the tangential direction) around the annulus comparing the uniform vane and multi-vane designs at an axial location midway between the OGV trailing edge and large pylon leading edge [3].

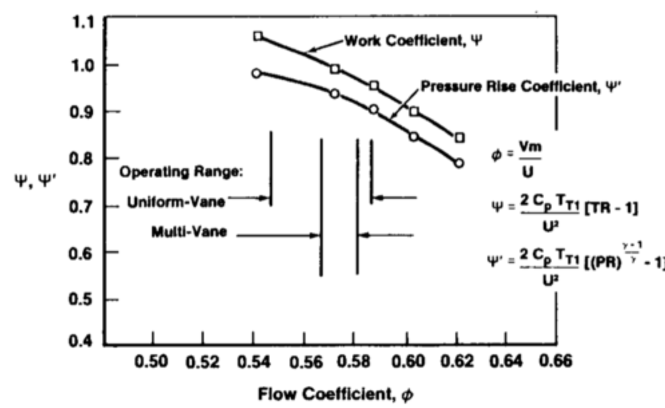

FIGURE 8: EEE fan rotor characteristic for a single speed line showing the range of flow coefficient for the uniform and multi-vane designs [3].

where δP_1 and δP_2 are the static pressure variation at the leading edge and trailing edge respectively. For this figure and the real engine hardware, the trailing edge flow angle was 0 deg. This amplification of the distortion can be seen in Figure 12 where the tangential static pressure distribution is plotted at an axial location just upstream of the vane leading edge plane for a case with and without the vanes. The case with the vanes has a lower average static pressure due to the turning. Both cases were run to the same mass flow. The case with vanes has a much larger variation in static pressure. One can even see the effects of the individual blades. From the simulation, the Amplification Factor is 1.33 whereas the ideal analysis produces a value of 1.6. The ideal analysis assumes zero attenuation whereas the finite chord of the vane does lead to a reduction of the Amplification Factor. There are 6 struts around the annulus in this configuration and it was the $6/rev$ crossing that created a rotor forced response issue. The amplification of the strut potential distortion exacerbated the problem.

There is an option within AEGIS to output the desired upstream flow angles that produces a uniform static pressure at the inlet plane upstream of a strut (or pylon). This output is then used to re-stagger the blades that will produce that upstream flow angle distribution. This option is demonstrated in Figure 13 which shows streamlines from the simulation downstream of the blades.

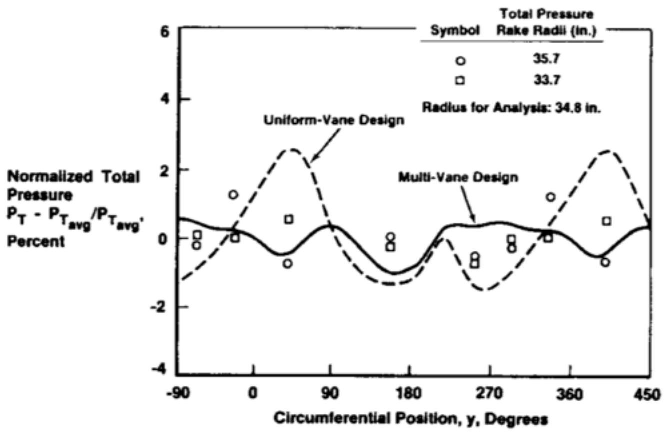

FIGURE 9: Comparison of Total pressure [3].

It can be seen how the optimized blades guide the flow around the strut. This almost eliminates the tangential static pressure variation at the inlet as shown in Figure 14. This optimized blade stagger solution would have been very effective, but a simpler solution of cutting back the strut leading edge was eventually chosen due to a lower cost. The enhanced understanding and possible mitigation approaches were made possible by a combination of analysis, computations, and tests.

I also wrote a 135 page user's manual [7] on the details of the input files and how to run the grid generator, the solver, and post processor. The input files for each blade were the same as used for the conventional blade-to-blade solver so the use of AEGIS by designers was relatively easy. The feedback from the designers in its use, including suggested improvements or enhancements, helped tremendously to have the code used for effective fan frames, struts, and blade-splitter applications.

♢ **Key Takeaway 1.** *Pylons and struts can cause large pressure variations that can impact the upstream rotor flowfield or increase the rotor unsteady stresses. A stator or OGV magnifies the pressure variation going upstream due to the diffusion of that blade row and the static pressure decreases going upstream. OGVs before a pylon often are designed with different camber and stagger around the annulus to guide the flow around the pylon.*

6 3D Isolated Blade Row RANS

General Electric's first production Reynolds Averaged Navier-Stokes (RANS) solver for Turbomachinery started out as an Euler Solver named Euler3D written by Graham Holmes and Siu Tong [8] who worked at what was then GE Global Research Center in Niskayuna, NY. Euler3D is an explicit single-block code using a five-stage Runge-Kutta time marching approach.

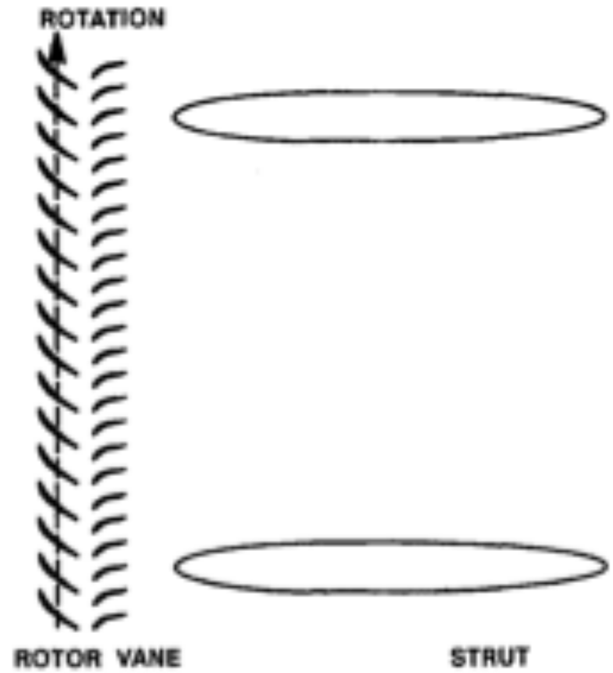

FIGURE 10: Schematic of the rotor, vane, and strut geometry for which the rotor blade had a forced response aeromechanics excitation [6].

The code was later modified at GE Aircraft Engines to include the added shear stress terms in the momentum equation and shear work and heat transfer terms in the energy equation. An algebraic Baldwin-Lomax turbulence model [9] as well as two k-ε turbulence models (the standard model [10] and extended model [11] were also added.

6.1 The Oxymoron, Viscous Euler

Since the Euler solver was modified to solve for viscous cases, it became convenient to name the code Viscous Euler (VE). It is recognized that this is in fact an oxymoron since Euler implies the flow is inviscid. One other semantic discussion is that since the turbulence model is applied for closure of the turbulent shear stresses, these codes are often described as solving the Reynolds Averaged Navier-Stokes Equations. The Reynolds averaging is strictly for incompressible flows. It is actually the Favre Averaging that is applied since the flows of interest are compressible. Because of this, there is a density fluctuation that needs to be accounted for in addition to the velocity fluctuations.

The first application of the VE solver was for transonic fans and presented in two papers from the 1992 Turbo Expo conference by Turner and Jennions [12] and by Jennions and Turner [13]. The conference papers were then published in the Journal

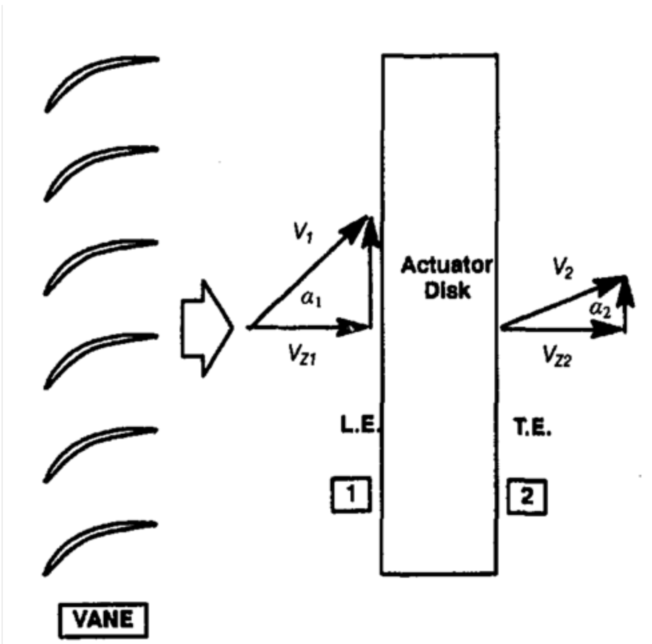

a) Schematic of actuator disk model

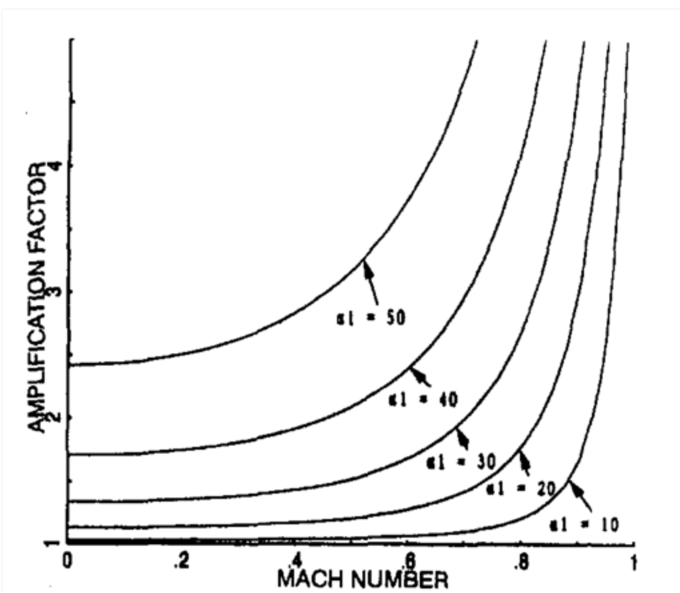

b) Model results with zero swirl at exit

FIGURE 11: Schematic of the Actuator Disk model of the vane (top) and the Amplification Factor (bottom) as a function of Machnumber and Leading Edge angle [6]. The trailing edge angle is zero for this analysis.

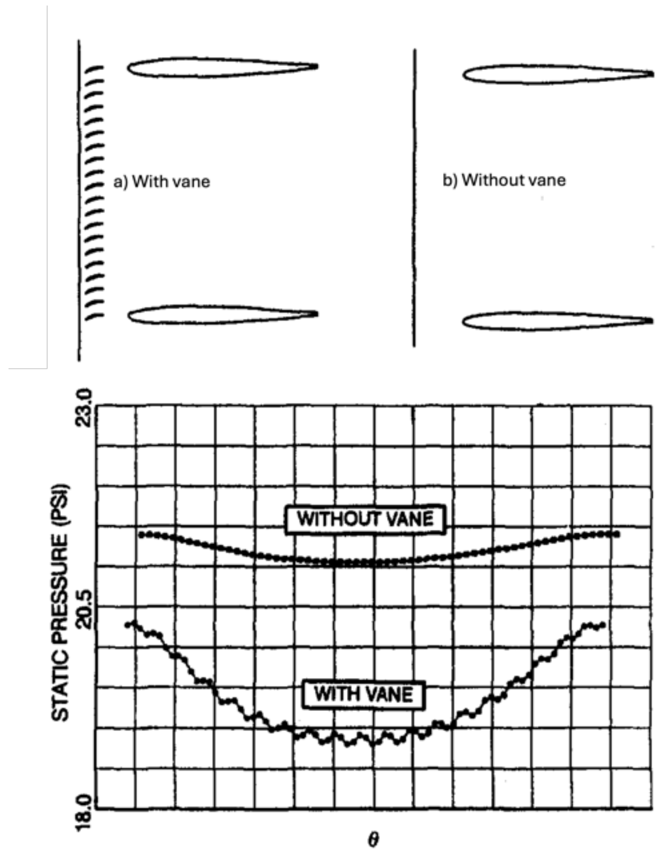

c) Tangential static pressure comparison at the same axial position.

FIGURE 12: Strut geometry with vanes (top left) and without vanes (top right) and the static pressure distribution at the plane location shown in the top plots which is the same distance upstream of the strut leading edge [6]. The static pressure is compared between the without vane and with vane case.

of Turbomachinery the next year.

A transonic fan was designed at GE Aircraft Engines and tested experimentally by Wennerstrom at Wright Patterson AFB. The fourth rotor in the sequence of fan rotors was simulated with the VE code and will be referred to as WR4. The simulations were run with three variations of an algebraic turbulence model developed by Balwin and Lomax [9] and two variations of the k-ε turbulence model (the standard model [10] and extended model [11]). Figures 15 and 16 show the grid for this WR4 case in the meridional plane (with a blowup of the tip region) and the blade-to-blade view (with a blowup of the leading edge), respectively. At the casing over the rotor tip, unsteady static pressure was measured with Kulite probes. This unsteady data was converted to the relative frame and time averaged and is shown in the

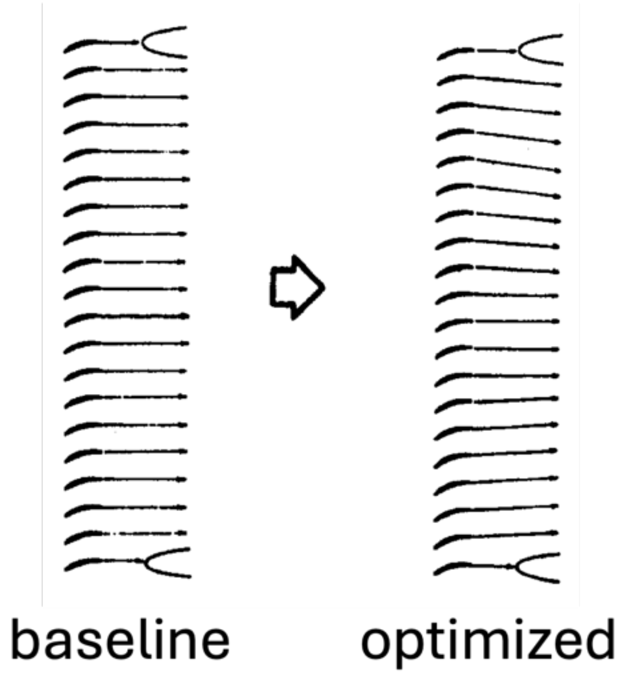

FIGURE 13: Streamlines from the stator trailing edge for the baseline, uniform case (left) and the optimized stagger case (right) [6].

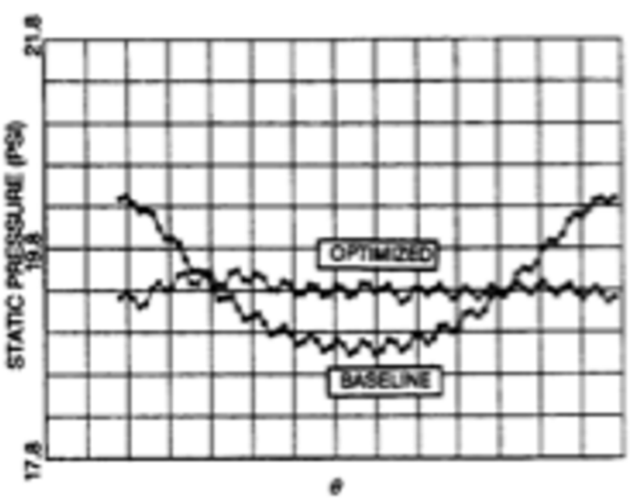

FIGURE 14: Static pressure distribution upstream of the stators with the baseline (uniform case) and the optimized stagger case showing the much reduced distortion that would be seen by the upstream rotor [6].

middle figure (b) of Figure 17 along with the contours of static pressure for the k-ε extended model at the bottom (c). The upper figure (a) shows a schematic of the features over the tip including the vortex, leading edge shock and diffuse passage shock. It can be seen that the simulation shown in (c) compares well with the experiment shown in (b). A line plot of the average static pressure is shown in Figure 18 for the different turbulence model simulations and are compared with the experimental results. This plot shows that the location of the shocks is simulated well with the k-ε models and that the extended model is slightly closer to the data. It is critical for the simulation to have the correct blockage from the boundary layers for which the turbulence model plays a big role. The shock structures are highly three-dimensional in a transonic fan, and contribute significantly to the entropy production within the rotor passage. It becomes critical that the solver used for design can accurately assess this blockage and therefore the correct shock structure.

Figure 19 shows radial profiles of efficiency comparing the simulations with different turbulence models with experimentally derived data. Both of the k-ε models compare well with the extended model picking up a bit more loss in the tip region.

Entropy is the appropriate property to assess loss as explained by Denton [14]. Since the inlet conditions were uniform P_T and T_T, these values were used to assign a zero value for entropy. The entropy function $\exp\left(-\frac{\Delta s}{R}\right)$ is a useful quantity since it is similar to total pressure for a stationary blade row. Contours of this entropy function are shown in Figure 20 where the smaller values represent higher loss and the region with a value at 1.0 is a loss-free core flow. The high loss regions are dominant near the tip and on the suction surface, which is typical for a transonic rotor. The turbulence model calculates values of turbulent viscosity μ_t. Sutherland's law is used to calculate the laminar viscosity, μ_l. This ratio of turbulent to laminar viscosity $\frac{\mu_t}{\mu_l}$ is a useful quantity to look at to assess the effect of the turbulence model. Figure 21 shows this ratio at midspan for the WR4 rotor for the simulation using the extended k-ε model. For this location and this turbulence model, the ratio varies between 100 and 600. The extended model had lower values of turbulent viscosity due to modified constants and an extra term in the dissipation (ε) equation that represents energy transfer rate from large-scale turbulence to small-scale turbulence.

Some people suggest that parameters within the turbulence models are "tuned" to help match the data. For the validation of the Wennerstom Rotor 4 and subsequent simulations, different turbulence models have been used for which there are physics that guides the choice of the model and what might be missing.

The paper by Jennions and Turner [13] presented the solution of three transonic fans. One was of the EEE fan, mentioned in the previous section. This geometry of the EEE fan is shown in Figure 22. The bypass OGV are the OGV's that were part of the fan frame simulation presented in the previous section. The domain that was simulated can be seen in the meridional

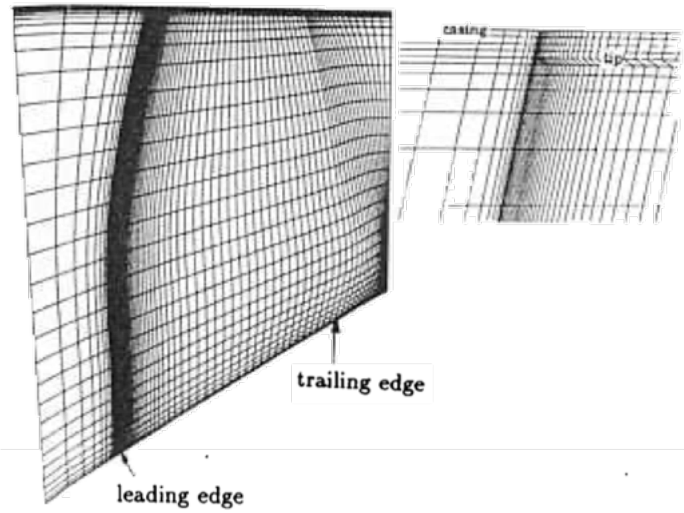

FIGURE 15: Meridional view of the Wennerstrom Rotor 4 (WR4) grid with a blowup of the tip gap [12].

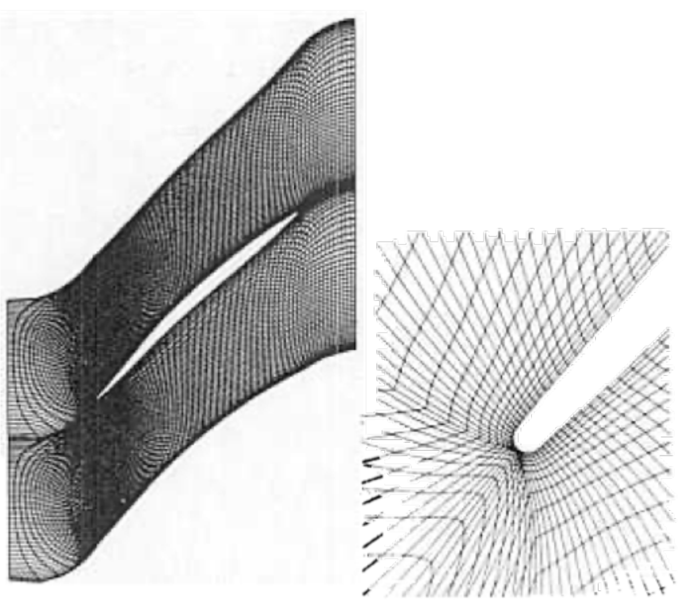

FIGURE 16: Blade-to-blade view of the WR4 grid with a blowup of the leading edge [12].

grid shown in Figure 23. One option in VE was that source terms could be calculated in different regions of the code from the initial conditions established. The initial conditions for this case came from a throughflow (axisymmetric) data match. The booster vane and booster rotor regions were then set to have the source terms calculated. This is done by calculating the residuals of the flow solver with the given flow quantities and those residu-

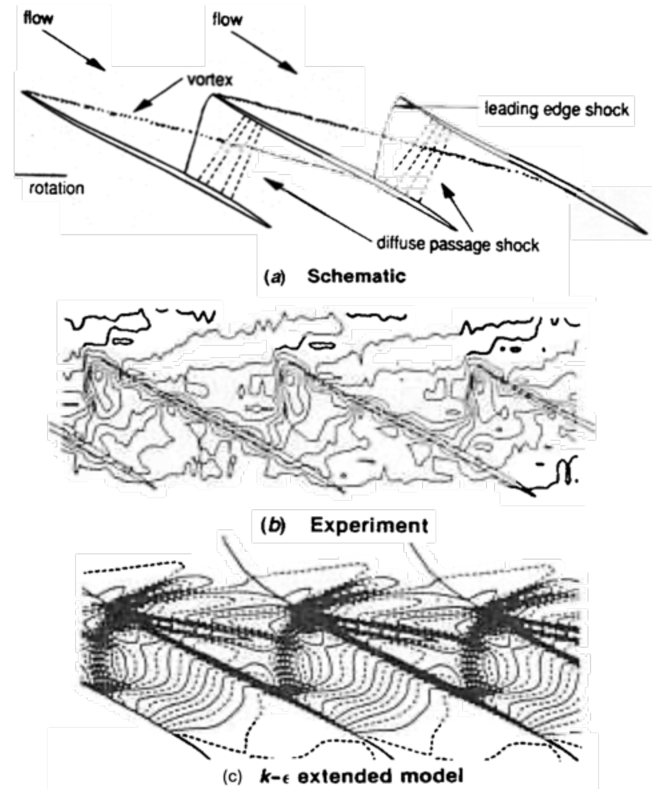

FIGURE 17: Static pressure contours at the casing for the WR4. a) is a schematic of the flow features b) is from the measured Kulite data, and c) is from the simulation. [12].

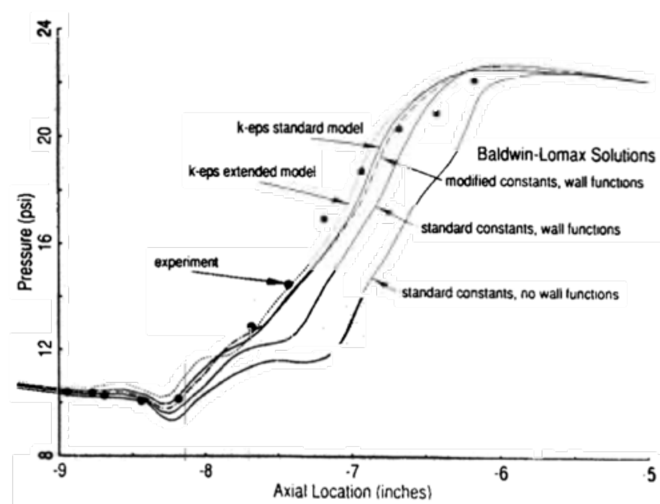

FIGURE 18: Tangentially averaged static pressure for the WR4 [12].

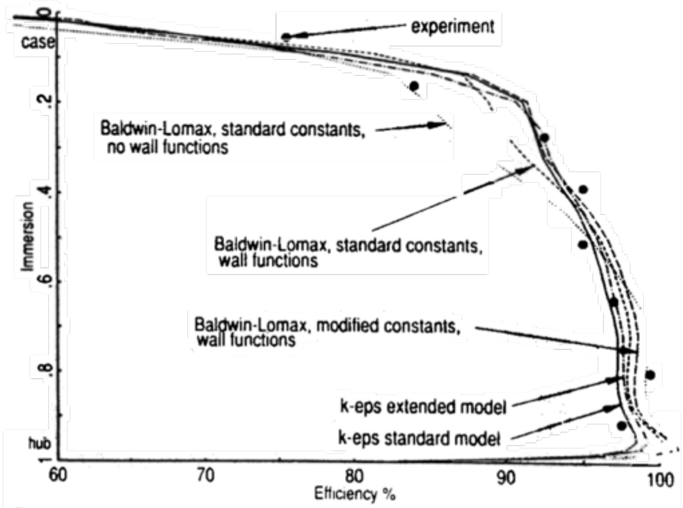

FIGURE 19: Radial profiles of rotor efficiency of the WR4 at the trailing edge plane comparing the different turbulence models with experimentally derived values [12].

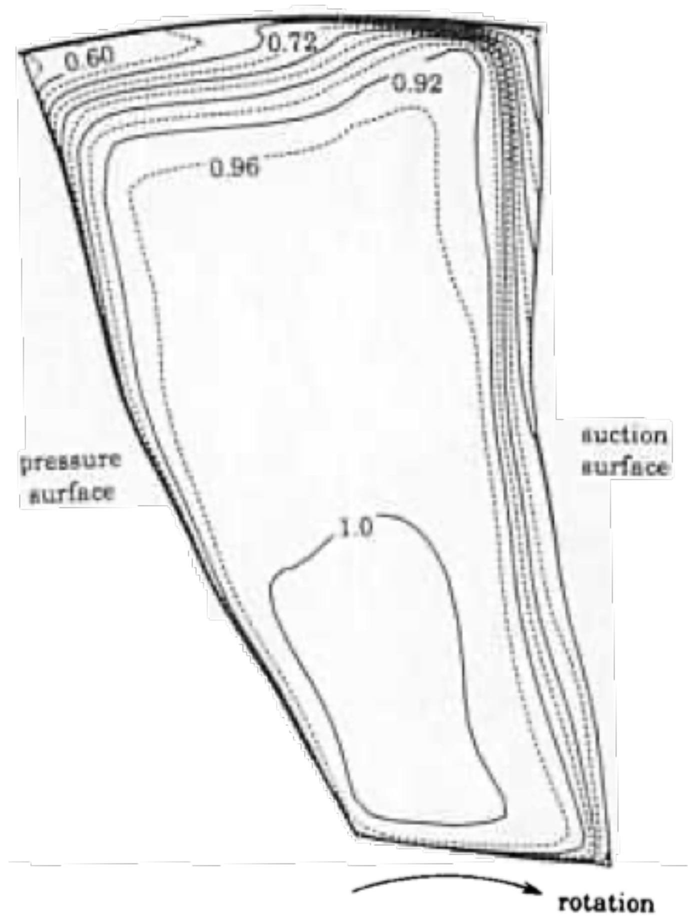

FIGURE 20: Contour plot of entropy function (exp $\left(-\frac{\Delta s}{R}\right)$) at the trailing edge plane for the WR4 using the standard k-ε turbulence model [12].

als then become the source terms. There will be more discussion about source terms in other sections.

For this simulation, the standard k-ε turbulence model was used with wall functions. Downstream, a simple radial equilibrium assumption was used to establish the static pressure profile while a static pressure was set in the bypass duct and downstream of the booster rotor to match flow rate and get the correct bypass ratio. Figure 24 shows a comparison between experiment and computed values of the normalized static pressure at the casing. A comparison between experiment and simulation of the tangential average static pressure is shown in Figure 25. There is excellent agreement. Profiles comparing experimental and simulation for total pressure and total temperature are shown in Figures 26 and 27 respectively. The comparison is very good.

The EEE fan had a part-span shroud although almost all subsequent fans did not since the technology then existed to eliminate them and improve performance. These excellent results of the fan simulations gave confidence in the use of the code for design for fans.

♢ **Key Takeaway 2.** *There are several key characteristics to have a CFD code become part of the design process for turbomachinery: accurate numerics, enforced conservation laws, validated results, include effects of turbulence, and effective documentation.*

VE was developed and only ever run as a single block solver. The part span shroud and engine splitter used triple grid lines that allowed boundary conditions to be set on solid boundaries or to set repeating conditions when the grid lines overlap. Turbine design incorporating 3D aero philosophies became extremely important after the validation of VE for transonic fans. However, the high exit angles and high Mach numbers of the high pressure turbine led to issues that needed to get resolved in order to be used for design. It is well known that highly sheared meshes can cause problems and can causes a loss of accuracy. A paper by several authors and me [15] explains how badly the shear can affect the solution for a very simple duct with a 3° ramp. The example is inviscid with a supersonic ($M = 1.2$) inlet. There is a shock at the start of the ramp followed by subsequent expansion and reflections. Figure 28 shows the Mach contours with the grids with different amounts of shear. It is clear that shear of 70° greatly reduces the accuracy and that 80° of shear almost eliminates the reflections. Figure 29 is a plot of the static pressure rise across the first shock as a function of the grid shear angle. It is clear from this plot how the shock jump is a large function of the grid shear and how the grids need to be more orthogonal to accurately capture the shock for these high turning turbine blades.

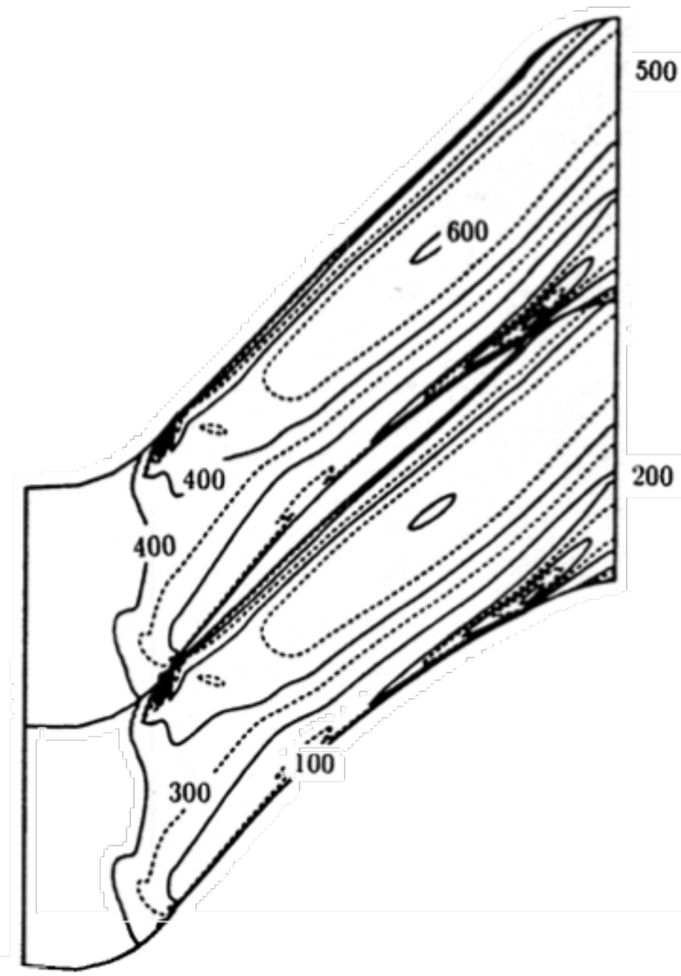

FIGURE 21: Contour plot of turbulent to laminar viscosity ratio ($\frac{\mu_t}{\mu_l}$) for the WR4 using the extended k-ε turbulence model [12].

The solution to reducing the high shear, while still maintaining the single block grids in VE was the I-grid. This is shown in Figure 30 with the full vane on the left and a zoom of the grid on the right. An elliptic grid generator was used and the near-orthogonality of the grids are apparent. At the periodic boundary, there is now a grid mismatch. The triple grid line approach was used to model the blade. Conservation of mass, momentum, and energy is critical for accurately predicting internal flows. One issue is that voids can occur in a grid if grids are snapped to a common curve as shown in the upper top image of Figure 31. To minimize the extent of the void, the grid is snapped to the grid line on the periodic boundary as shown in the bottom image of Figure 31. The VE algorithm is cell-centered so the periodic boundary condition sets "phantom" boundary cells based on the cells on the other side of the periodic boundary. The grids are constructed so they match on radial lines (each grid surface in

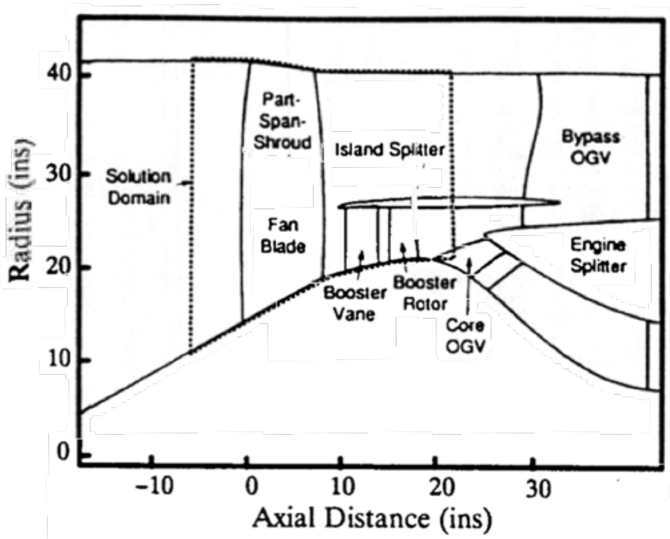

FIGURE 22: A meridional view of the geometry for the EEE fan simulation [13]. The booster vane and booster rotor are modeled as source terms.

the blade-to-blade direction is on a surface of revolution) and linear interpolation can be used. The interpolation is applied to the flow variables and at each multigrid level. Conservation is not guaranteed with this approach so the cumulative fluxes are linearly interpolated across each grid slab in 3D and the average boundary flux across the periodic boundary is enforced. This is applied for all fluxes and guarantees conservation.

A Von Karman Institute (VKI) nozzle guide vane (VKI-LS82) presented at a 1982 VKI workshop was used to demonstrate the benefits of the I-grid and also validate the code for a 2D geometry. The vane has a trailing edge exit angle of approximately 80°. The grid for this case is shown in Figure 30. The LS82 case was run at several different back pressures corresponding to the isentropic exit Mach number. The comparison between the simulations and experimental results are shown in Figure 32, showing very good agreement. Also in the figure are the Mach number contours for the 1.43 exit Mach number case. The shocks and shock reflections can be seen clearly. The benefit of developing the I-grid capability can be understood by referring to Figure 33. The I-grid with nbb=48 (nbb is the number of blade-to-blade cells) matches the experiment very well and so does the simulation with half the number of blade-to-blade cells (nbb=24). With the highly sheared H-grid and nbb=24, the high isentropic Mach number at 43% chord is totally missed. Even with nbb=48, the value of isentropic Mach number is lower than the experimental value with the H-grid.

A 2D validation case is necessary, but not sufficient to validate a code and methodology, especially since it is for 3D design of turbine vanes and blades that the I-grid code was to be used.

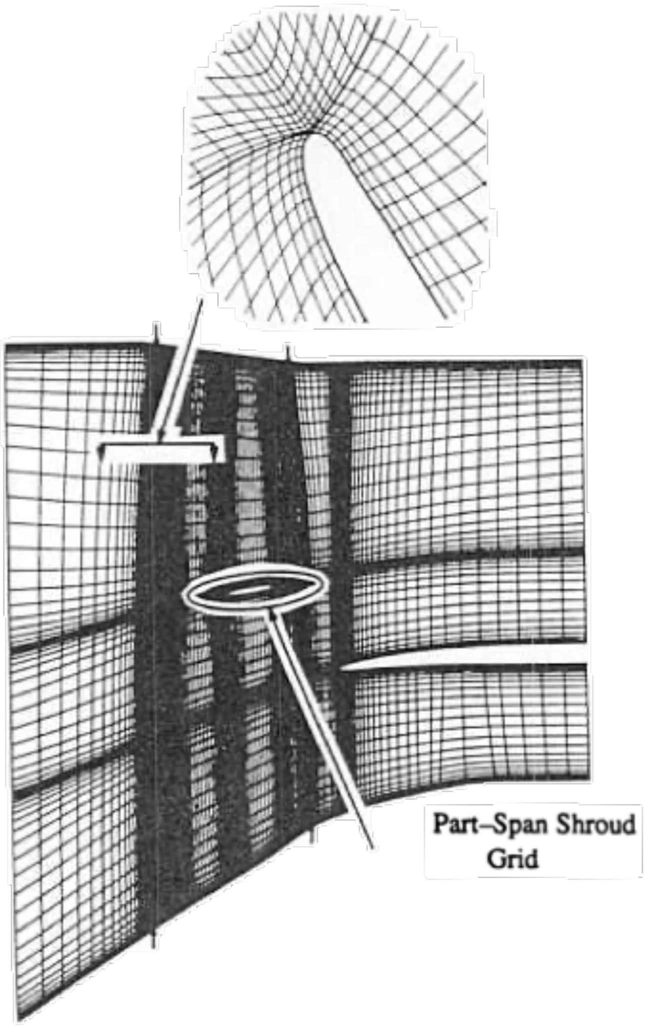

FIGURE 23: The meridional view of the EEE fan grid [13]. The top grid is a blowup of the leading edge of the fan.

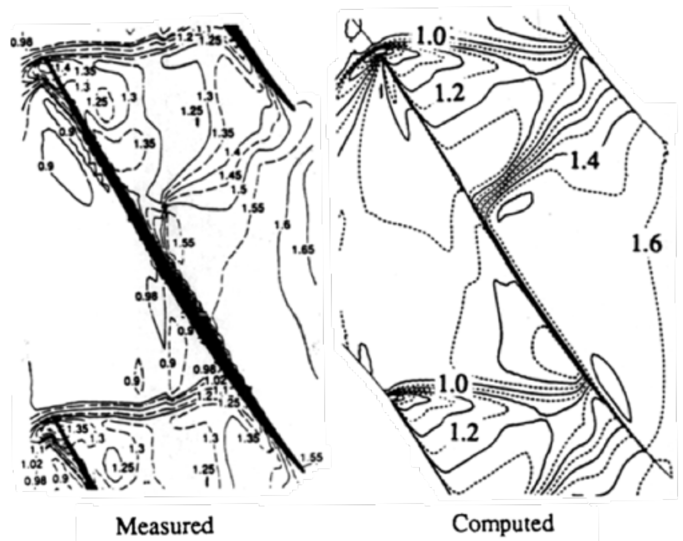

FIGURE 24: EEE casing normalized static pressure contours [13].

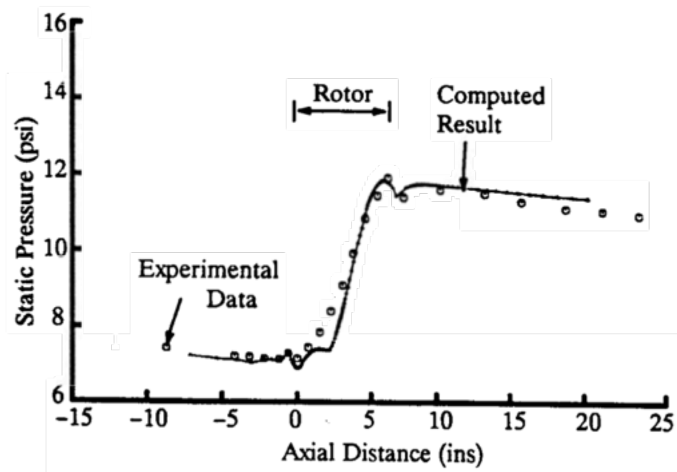

FIGURE 25: Tangentially averaged static pressure at the casing [13].

Two HPT vane designs had been tested in an annular cascade rig. The HPT first vane is typically cooled, and the experiments that are used for comparison have cooled blades, but no band or endwall cooling. The simulations did not model the cooling flow in the vane. The first tested vane was the Low Aspect Ratio (LAR) vane that was typical of production at the time. The other was the Advanced Turbine Nozzle Aerodynamics (ATNA) vane that was representative of an advanced 3D vane, and also included contoured endwalls. Both vanes had trailing edge flow angles approaching 80° and had design trailing edge Mach numbers that were supersonic. The rig schematic and blade geometry for both LAR and ATNA are shown in Figure 34. Figure 35 compares the total pressure contours at the exit plane for the ATNA experimental results and the simulation with VE using an I-grid. The 3D nature of the blade geometry effect downstream can be observed based on the 3D nature of the vane wake. There are some discrepancies most likely due to the cooling flow on the blades in the experiment and some turbulence modeling deficiencies, but overall the shape and high loss magnitudes are comparable. The profiles of circumferential averaged total pressure are shown for LAR and ATNA and compares the experimental and simulation results. The comparison is adequate considering the lack of cooling flow in the simulation. It does demonstrate the higher total pressure near the casing with the ATNA design that was the desired feature of the design. It would have been best to have a simulation that exactly modeled the experiment, but the model-

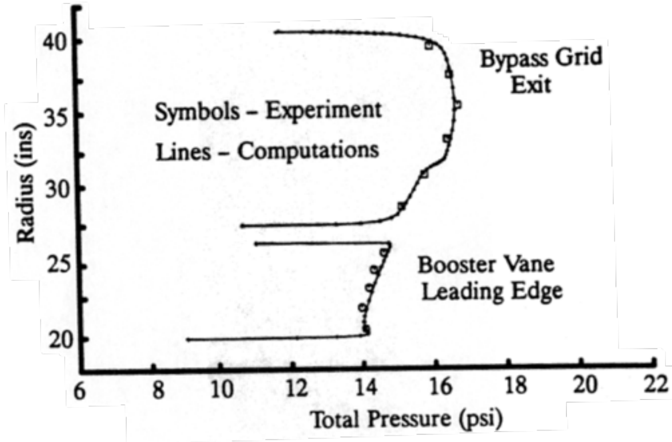

FIGURE 26: Profile of the downstream total pressure comparing experiment with computation [13].

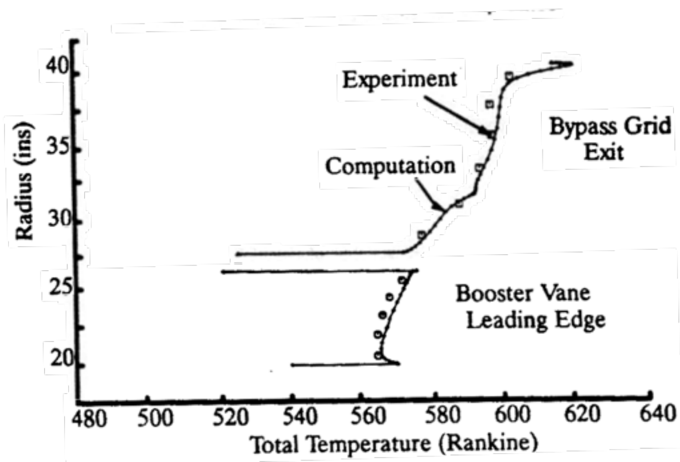

FIGURE 27: Profile of the downstream total temperature comparing experiment with computation [13].

ing of cooling flows had not yet been added to VE. Since the LAR and ATNA were such different designs, the difference in the simulations and experiments could be ascertained. The benefit of the I-grid has been the ability to more accurately capture shocks with high trailing edge angles. The suction side shocks of the vane going downstream are shown in the Mach contours of Figure 37 for both LAR and ATNA.

Figure 37 also demonstrates how the exit boundary condition that was applied allows for the shock to exit downstream through the boundary with little to no reflection. The values of static pressure (P_s) just upstream of the downstream boundary are used to set the downstream boundary phantom points. Then the tangentially averaged P_s is calculated at each span. The boundary condition is a radial profile of tangentially averaged P_s. The downstream values are all modified by adding the difference between the target Ps and the calculated P_s. This then allows the tangential variation of P_s to exit the domain.

The I-grid capability along with the validation to experimental results allowed for turbine designers to take advantage of the CFD capability for creating 3D aero designs that would be part of an engine.

◇ **Key Takeaway 3.** *A simple canonical problem such as the duct with a supersonic inlet and a ramp can be very useful for understanding numerical algorithms and how to address various issues.*

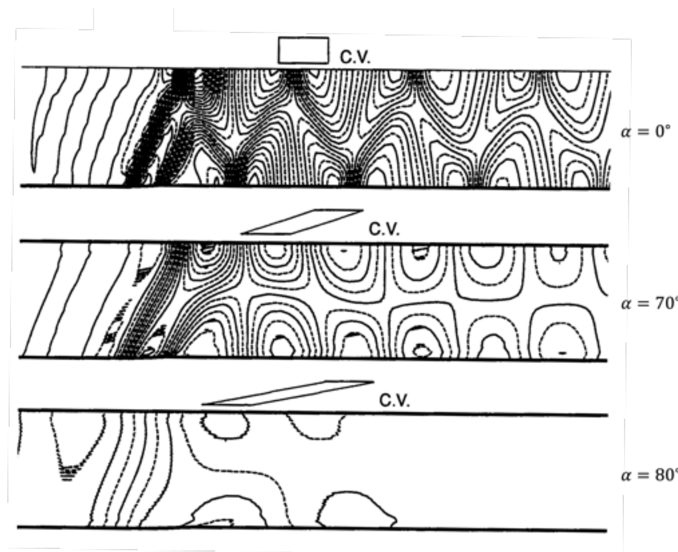

FIGURE 28: Effect of sheared grid for simple duct problem [15].

7 Multistage Simulations Using Average Passage

The Average Passage method was developed by John Adamczyk [16], and models adjacent blade rows using source terms that get evaluated from a closure model. Dr. Adamczyk discussed how the Average Passage approach could be used to support design in a Scholar Lecture 25 years ago [17]. There have been many other papers written about the results from using the Average Passage formulation developed by Adamczyk [18] [19] [20].

Kevin Kirtley, Sohrab Saeidi, and I published a paper in 1999 [21] that describes a modification of the closure for the Average Passage method that allows for improved grids. That paper explains how the original closure requires pure H-grids as

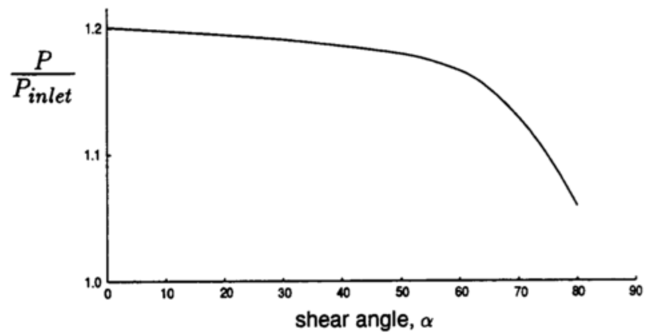

FIGURE 29: Static pressure rise across the first shock for the simple duct problem as a function of the grid shear [15].

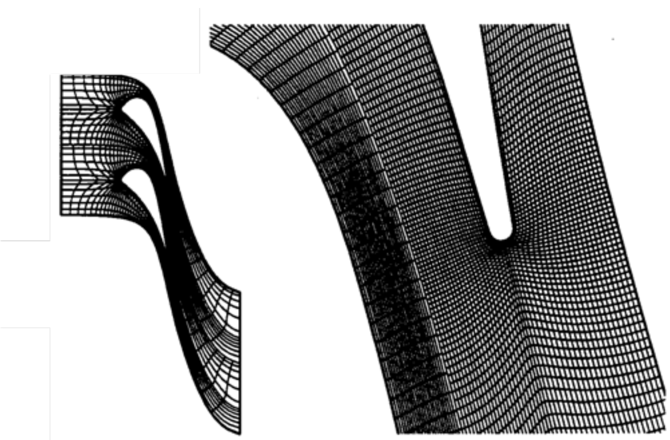

FIGURE 30: I-grid for a vane. Every 4th grid line shown on the left and a zoom of the throat region on the right [15].

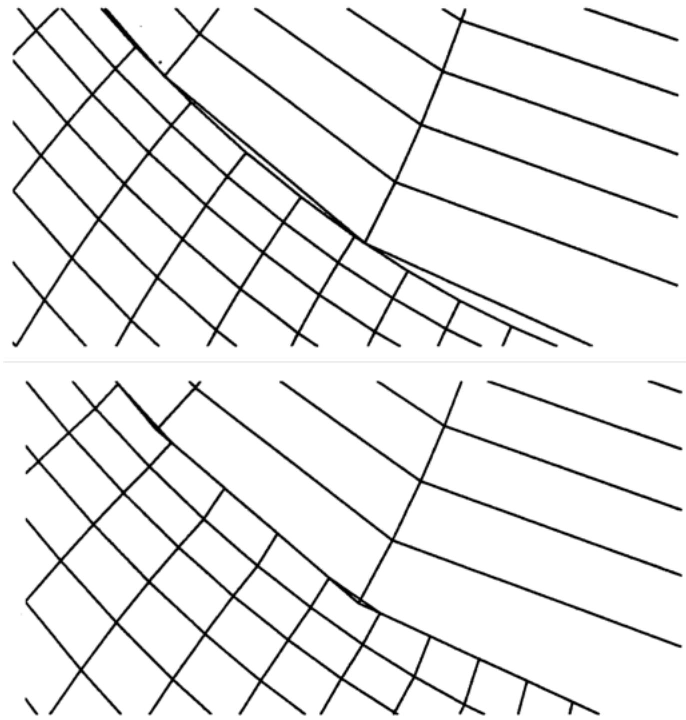

FIGURE 31: I-grid interface with points snapped on a curve (upper figure) or snapped to the adjacent periodic grid (lower figure) [15].

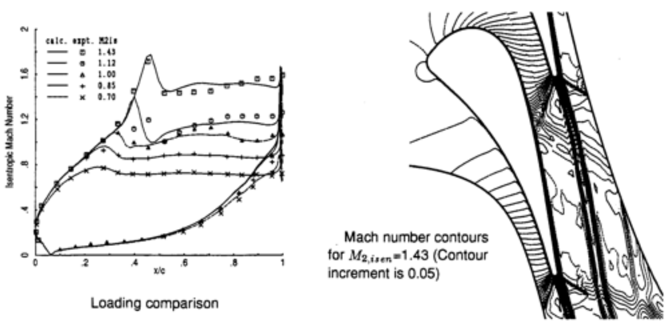

FIGURE 32: VKI-LS82 I-grid results with a comparison to experimental results on the left and Mach contours for the exit Mach of 1.43 on the right [15].

shown in Fig. 38 with a zoom of the leading edge shown in Fig. 39. The pure H-grids have high shear and, as was demonstrated with the development of the I-grid in the previous section, the high shear can cause issues with the numerical simulations. The paper describes the details of the more general closure for non-pure H-grids, and part of that explanation is repeated here. One of the features of the more general closure is that is reverts to the traditional closure if the pure H-grids are used.

With the Average Passage model:

1. A 3D solution is generated for every blade row that includes adjacent blade rows as well as an axisymmetric solution
2. Both the 3D equations of adjacent blade rows and the Axisymmetric or 2D equations contain the physical blade blockage factor λ
3. The source terms applied to the 3D equations and the Axisymmetric equations are the difference between the 2D residuals evaluated using the axisymmetric average solution and the average 3D residuals
4. Because the solution vector is $\rho\vec{V}$, then the source terms for the continuity equation should be zero
5. The closure is applied to the radial and axial momentum equations, the angular momentum equation, the energy equation, the equation of state, and the k and ε turbulence equations
6. The source terms for each blade row represent a field in the

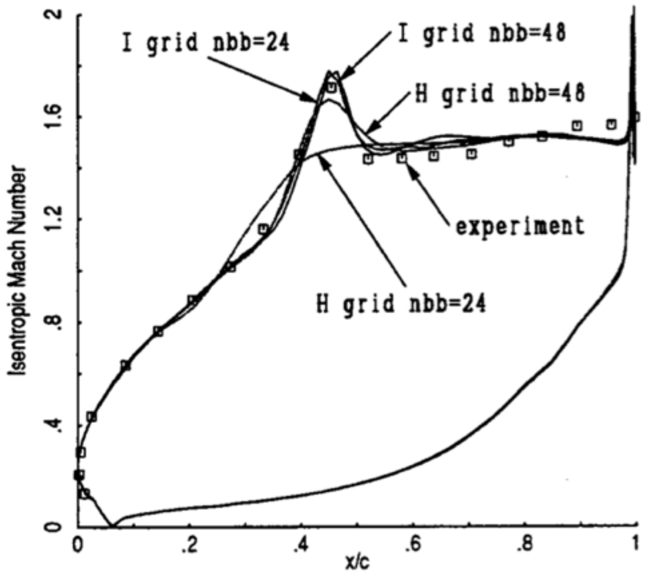

FIGURE 33: The loading distribution for the VKI-Ls82 case at an exit Mach number of 1.43 using different grids and compared to experiment [15] (nbb is the number of blade-to-blade cells).

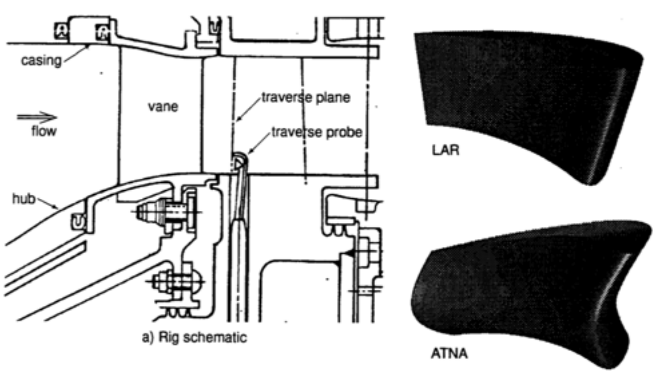

FIGURE 34: High pressure turbine nozzle cases LAR (Low Aspect Ratio) and ATNA (Advanced Turbine Nozzle Aerodynamics). Rig flowpath schematic on left and nozzle 3D geometry on right [15].

Axisymmetric domain. They are applied uniformly in the tangential direction in 3D.

The Average Passage model has also been defined with equations and presented by Kirtley et al. [21]. The following set of equations are a condensed version of what that paper presented and using the same nomenclature.

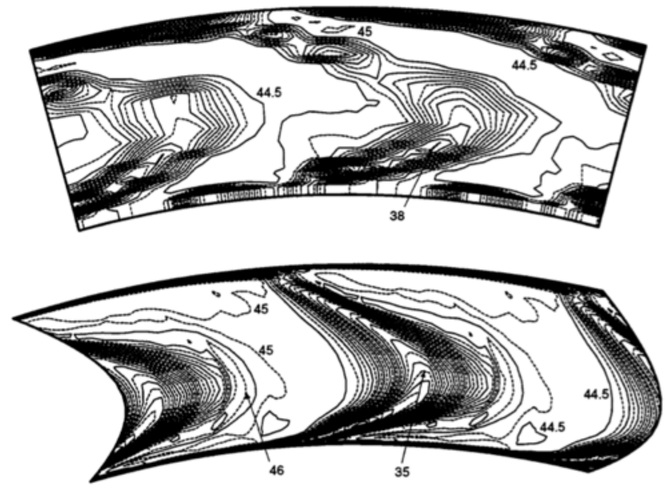

FIGURE 35: Contours of Total Pressure downstream of ATNA vane at the measurement plane, experimental above and computation below [15]. Contour intervals are 0.5 psi.

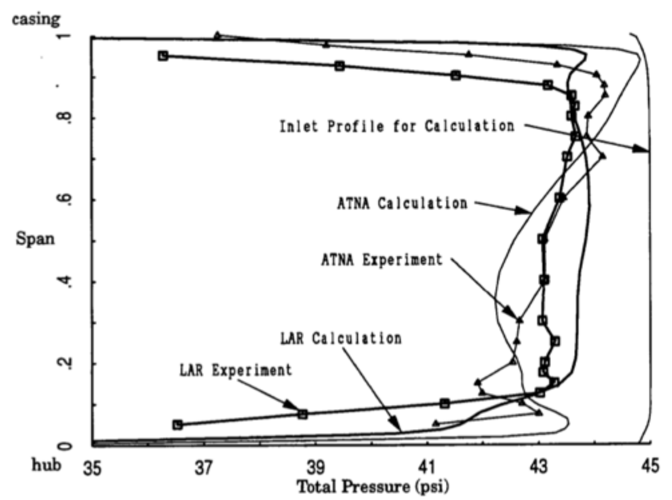

FIGURE 36: Profiles of total pressure for the LAR and ATNA vanes at the exit plane for experiment and simulation [15].

The axisymmetric average is defined as

$$\mathbf{q_a} = \frac{\int \mathbf{q_{3d}} \mathbf{d}\theta}{\int \mathbf{d}\theta} = \mathbf{A}\mathbf{q_{3d}} \tag{2}$$

where $\mathbf{q}$ is the solution vector and $\mathbf{A}$ is the Axisymmetric averaging operator. Another operator, $\mathbf{P}$ is the injection operator that inserts any axisymmetric quantity into each point in the 3D computational domain. The difference, $\hat{\mathbf{q}}$ between the passage

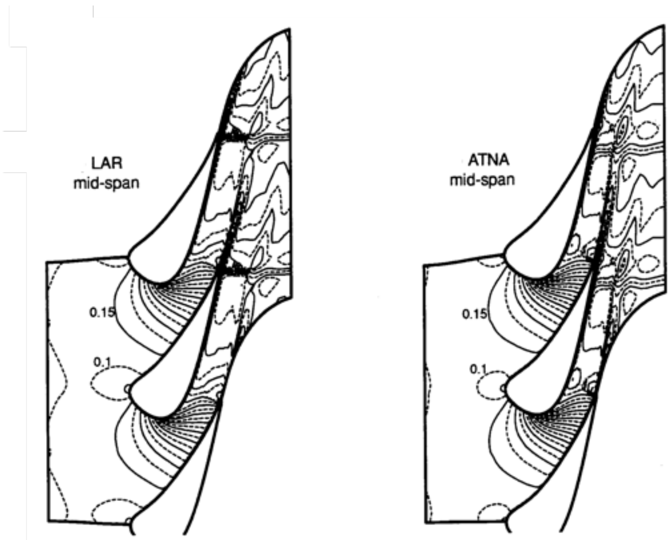

FIGURE 37: Mach number contours from the simulations of the LAR and ATNA vanes at mid-span [15]. Contour intervals are 0.05.

average steady 3D vector and its axisymmetric average is

$$\hat{\mathbf{q}} = \mathbf{q_{3d}} - \mathbf{PAq_{3d}} \tag{3}$$

The axisymmetric average of $\hat{\mathbf{q}}$ is identically zero so therefore

$$\mathbf{A}\hat{\mathbf{q}} = \mathbf{Aq_{3d}} - \mathbf{APAq_{3d}} = \mathbf{0} \tag{4}$$

which is only valid if $\mathbf{AP} = \mathbf{I}$. Kirtley et al. [21] explains that $\mathbf{P} = \mathbf{A^{-1}}$ can only be valid for pure, coincident H-grids. For these pure H-grids, the closure model for the i^{th} blade row is:

$$\frac{\partial\left(\lambda^{\mathbf{i}}\mathbf{q^i_{3d}V^i_{3d}}\right)}{\partial \mathbf{t}} + \mathbf{N_{3d}}(\lambda^{\mathbf{i}}\mathbf{q^i_{3d}}) = \sum_{\mathbf{j \neq i}}^{\mathbf{M}} \mathbf{B^j} \tag{5}$$

where N_{3d} is the Navier-Stokes operator in 3D and the deterministic source term $\mathbf{B^i}$ is

$$\mathbf{B^i} = \mathbf{N_{2d}}(\lambda^{\mathbf{i}}\mathbf{q^i_a}) - \frac{\mathbf{1}}{\theta_{\mathbf{pitch}}}\int_{\theta_{\mathbf{min}}}^{\theta\mathbf{max}} \mathbf{N_{3d}}(\lambda^{\mathbf{i}}\mathbf{q^i_{3d}})\mathbf{d}\theta \tag{6}$$

where N_{2d} is the axisymmetric Navier-Stokes operator (in 2D). The derivation of B comes from the condition of a unique throughflow representation:

$$\mathbf{q_a} = \mathbf{q^1_a} = \mathbf{q^2_a} = \ldots = \mathbf{q^M_z} \tag{7}$$

where q_a is the solution of the throughflow equation:

$$\frac{\partial\left(\lambda \mathbf{q_a V^i_{2d}}\right)}{\partial \mathbf{t}} + \mathbf{N_{2d}}(\lambda \mathbf{q_{2d}}) = \sum_{\mathbf{j}}^{\mathbf{M}} \mathbf{B^j} \tag{8}$$

For a general mesh, $\mathbf{AP} \neq \mathbf{I}$ and the averaging operator $\mathbf{A}$ is based on an conservative method developed by Dukowicz [22] for interpolating to a pure H-grid using a conservative approach. The prolongation or injection operator is also applied with the Dukowicz algorithm, but interpolating for the axisymmetric mesh to the 3D mesh. In the computer code]**A** and **P** are stored as a linked list of weights and pointers for the interpolation. Details are found in Kirtley et al. [21]. Because $\mathbf{AP} \neq \mathbf{I}$, there is discretization error. To ensure that these errors go to zero for the whole domain, the concept of rectifying cells was introduced. This is shown in Figure 40 where in between blade rows the 3D meshes and the axisymmetric meshes have coincident pure H-grids. These cells will ensure that the discretization errors are kept to each blade row. The closure for the generalized grids is represented by the following equations.

$$\frac{\partial\left(\lambda^{\mathbf{i}}\mathbf{q^i_{3d}V^i_{3d}}\right)}{\partial \mathbf{t}} + \mathbf{N_{3d}}(\lambda^{\mathbf{i}}\mathbf{q^i_{3d}}) = \mathbf{P^i}\sum_{\mathbf{j \neq i}}^{\mathbf{M}} \mathbf{B^j} \tag{9}$$

$$\mathbf{B^i} = \mathbf{N_{2d}}(\mathbf{A^i}\lambda^{\mathbf{i}}\mathbf{q^i_a}) - \mathbf{A^iN_{3d}}(\lambda^{\mathbf{i}}\mathbf{q^i_{3d}}) + \mathbf{A^iP^i}\sum_{\mathbf{j \neq i}}^{\mathbf{M}} \mathbf{B^j} - \sum_{\mathbf{j \neq i}}^{\mathbf{M}} \mathbf{B^j} \tag{10}$$

It turns out that for pure H-meshes, this general closure reverts to the original closure.

The benefit of the general closure can be seen by the improved grids that can be used as shown in Figure 41 with a zoom of the leading edge in Figure 42. The general closure was compared to the original closure using a 2 1/2 stage low pressure turbine described by Halstead et al. [23] and in Scott Hunter's Ph.D. dissertation [24]. The non-pure H-grids improve convergence relative to the pure H-grids as shown in Figure 43, which shows the $L2$ norm of the residuals. The solutions using the non-pure H-grids are also improved as seen in Figure 44 comparing the P_T profile downstream of the second vane and in Figure 45 showing the P_T downstream of blade 2. The profiles compare more favorably to experiment with the non-pure H-grids using the more generalized closure.

The Average Passage formulation allows for adjacent blade rows to affect the multistage simulation by having the adjacent metal blockage, with its associated back pressure affect, the turning, which in turn changes the streamline curvature in both the meridional plane and blade-to-blade. It also allows for the wakes to be turned by the average flowfield and to continue to dissipate. The closure means that the axisymmetric average of each blade row is the same, and does not produce a jump across an interface plane like a mixing-plane approach would do.

♢ **Key Takeaway 4.** *The Average Passage approach for multistage turbomachinery simulation allows for rapid and accurate results that include many of the blade row interaction effects. Allowing more orthogonal grids with the general closure has enabled the approach to be used effectively in design.*

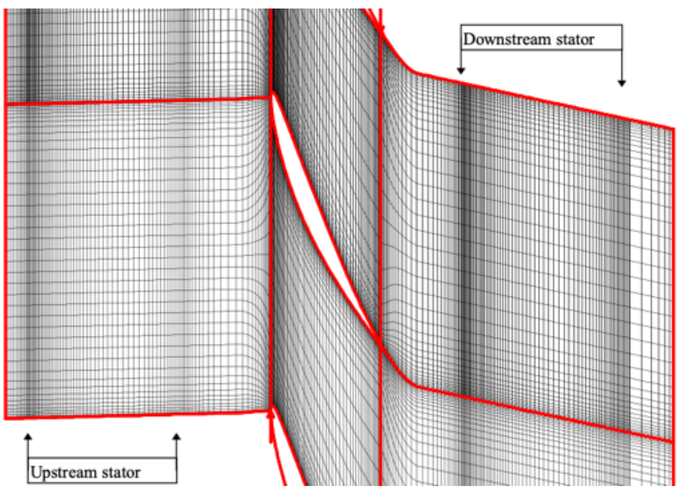

FIGURE 38: Pure H-grid used for original APNASA closure with compressor rotor and overlapping domains with the upstream and downstream stators [21].

7.1 Source terms, blockage and the AP closure

The
FIXXXXXXXX

7.2 Full Engine Simulation of the GE90

At the time the general closure of the Average Passage formulation was implemented, the design of the GE90 was taking place. Because of the timeliness of the design and easy access to design geometry and conditions, I promoted the idea to GE that we work with NASA to simulate the entire GE90 in 3D encompassing all 50 blade rows. As mentioned by Robert Garvin in his book [25], the "new GE90 for the Boeing 777, which uses the complete E Cubed high-pressure compressor more or less unchanged." Because of the large size of the GE90, the HPC was larger than the EEE (or E Cubed).

The fan, fan bypass with the nominal type of OGVs, and the booster would be simulated with the general closure form

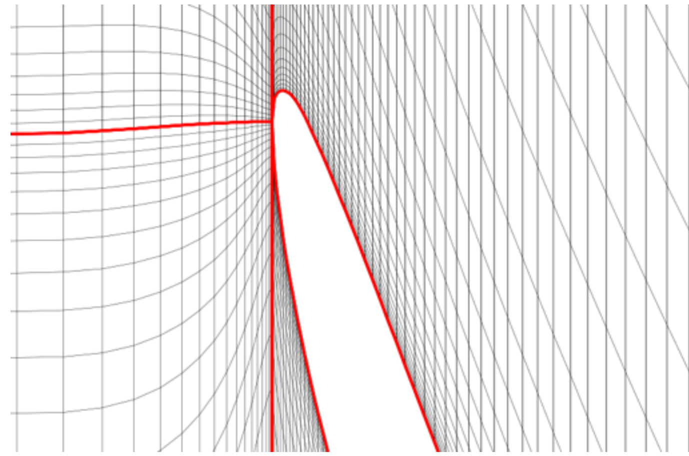

FIGURE 39: Zoom of the leading edge of a compressor rotor with pure H-grid [21].

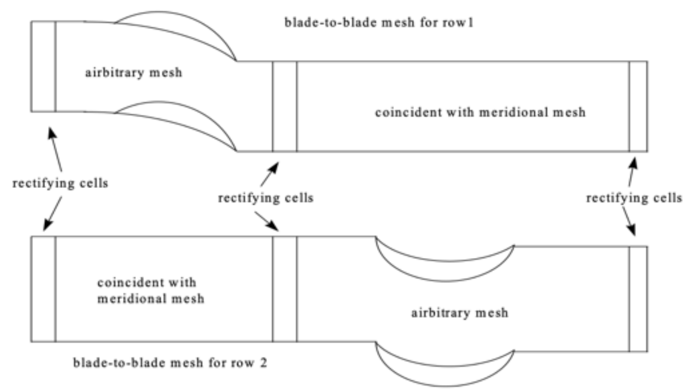

FIGURE 40: Schematic of the domains needed with the general APNASA closure that allows for non-pure H-grids. The use of rectifying cells ensures any errors associated with interpolation with an arbitrary mesh will be contained in that blade row and conservation is guaranteed over the full domain [21].

of the Average Passage code. The HPC would be simulated with the original closure form of APNASA and many of the details of the GE90 HPC rig were described in the scholar paper by John Adamczyk [17] that has previously been mentioned. The combustor was modeled with the National Combustor Code (NCC) [26]. Both the cooled High Pressure Turbine (HPT) and Low Pressure Turbine (LPT) were modeled with the general closure form of the Average Passage code and presented by coauthors and myself [27].

The full engine simulations were published in several papers [28] [29] [30] [31] [32].

In the 2010 AIAA paper, I published the lessons learned from the GE90 3D Full Engine Simulations [32]. That publi-

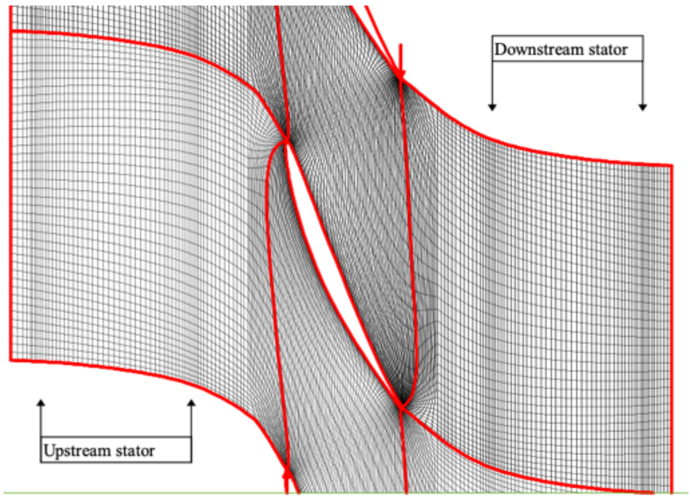

FIGURE 41: Elliptic grid used in the non-pure H-grid region of the compressor rotor while pure H-grids are used in the rectifying cells and the region of the upstream and downstream stators [21].

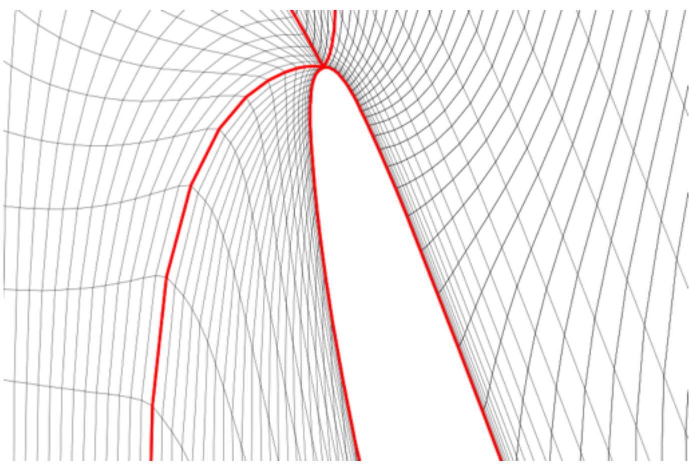

FIGURE 42: Zoom of the leading edge of a compressor rotor with non-pure H-grid [21].

cation describes the advances and impact that the work had and how it can be used to impact the design and understanding of component coupling and engine design.

♢ **Key Takeaway 5.** *The full engine simulation of the GE90 proved that such a large and complicated simulation could be done in 3D. It paved the way for other full engine simulations and more component coupling. It was critical that the GE90 was an active engine development project at the time so geometry and test data was readily available.*

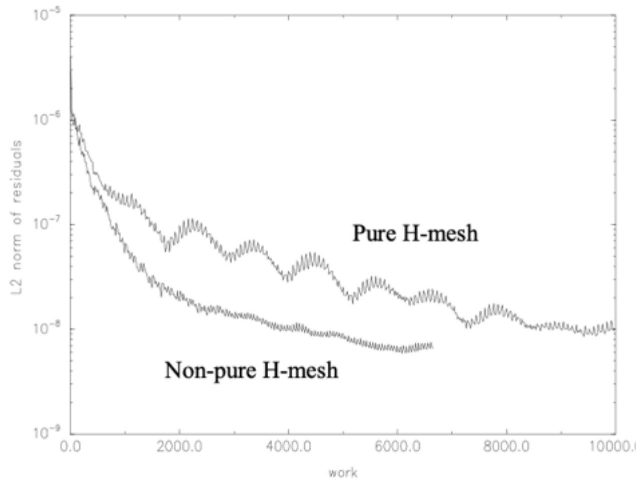

FIGURE 43: Comparison of the $L2$ norm of the residuals when running APNASA with a pure H-grid and non-pure H-grid [21].

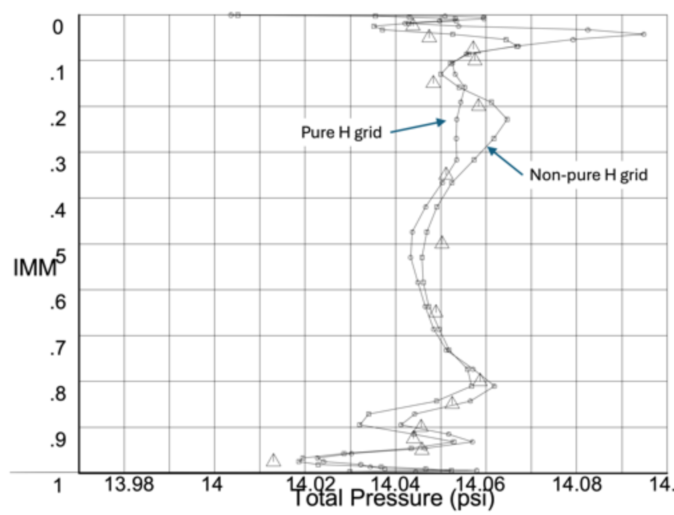

FIGURE 44: Comparison between experiment, pure-H grid and non-pure H-grid solutions of the total pressure profile downstream of vane 2 for the 2-stage turbine [21].

8 Reynolds Averaged Navier-Stokes (RANS) and Favre Averaged Navier-Stokes

8.1 Assumption of RANS

8.2 Reynolds Analogy

8.3 Wall Functions including Roughness

[33]

$$u^+ = \frac{1}{\kappa} ln(y^+) + D. \tag{11}$$

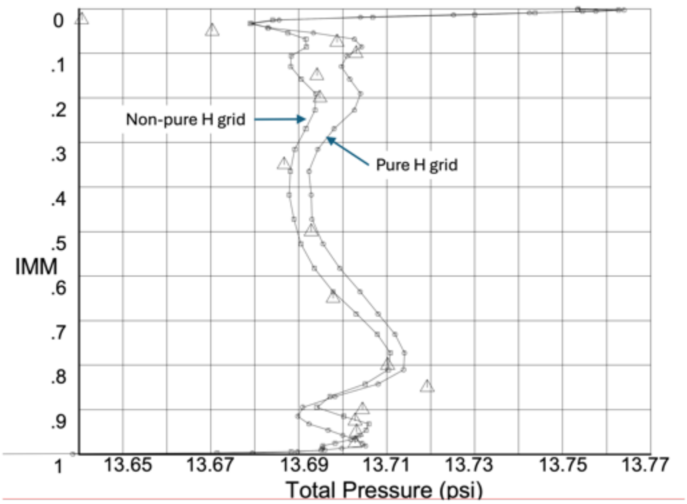

FIGURE 45: Comparison between experiment, pure-H grid and non-pure H-grid solutions of the total pressure profile downstream of rotor 2 for the 2-stage turbine [21].

$$y^+ = u^+ + e^{-\kappa D}\Big[e^{\kappa u^+} - 1 - \kappa u^+ - \frac{(\kappa u^+)^2}{2} - \frac{(\kappa u^+)^3}{6}\Big] \quad (12)$$

$$D = B - 2.5ln(k_s^+) \quad (13)$$

where B is a new coefficient and has been determined experimentally for a range of values of surface roughness, k_s. For hydraulically smooth and rough surfaces B is a function of k_s^+ but for a completely rough surface it is a constant with an average value of 8.5. For the results shown later in the paper, B in this regime was obtained from Schlicting [34].

As mentioned in our paper [33], we did not know who suggested to re-write Equation 12 in terms of skin friction coefficient C_f and the cell Reynolds number $Re = \rho y u/\mu$ where y is the distance between the solid surface and the cell center (vertex if a vertex scheme is used) of the first grid cell at the solid surface. Note that the velocity u in this Reynolds number is the local velocity at the cell center (or at the vertex).

By substituting the relations $y^+ = Re/u^+$ and $u^+ = \sqrt{2/C_f}$ into Equation 12, and re-arranging

$$Re = \frac{2}{C_f} + e^{-\kappa D}\Big[(\frac{2}{C_f})^{1/2} e^{\kappa\sqrt{\frac{2}{C_f}}} - (\frac{2}{C_f})^{1/2} - \kappa(\frac{2}{C_f}) - \frac{\kappa^2}{2}(\frac{2}{C_f})^{3/2} - \frac{\kappa^3}{6}(\frac{2}{C_f})^2\Big] \quad (14)$$

In a CFD code, Re is readily obtained, and we desire C_f.

In the appendix of the paper [33] is a short program is listed as an algorithm for getting C_f from Re.

◇ **Key Takeaway 6.** *It was extremely surprising to me that the Figure 48 pf C_f as a function of Re appears like the Moody diagram that Moody published in 1944 as shown in Figure 49 [35]. However, it should not have been that surprising since the rough pipe data and boundary layer data can collapse to similar curves using appropriate non-dimensional parameters, namely Re, C_f and $\frac{k_s^+}{y^+}$ or $\frac{\varepsilon}{D_h}$.*

test case [36] [37]

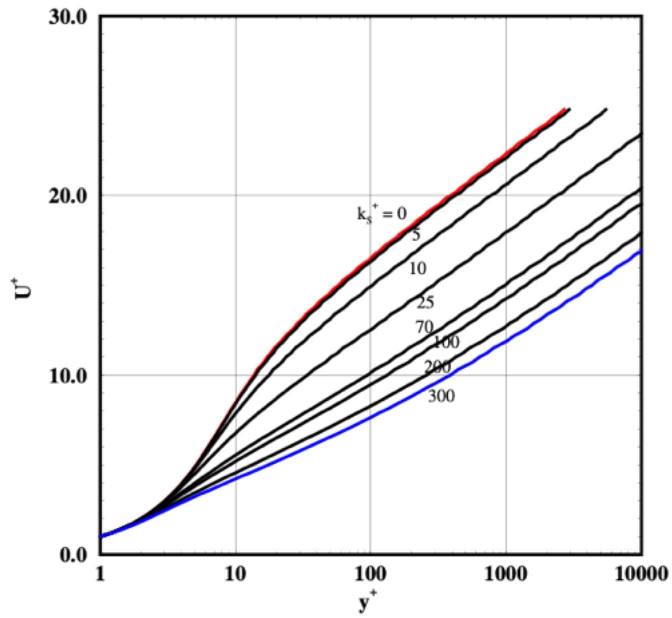

FIGURE 46: Plot of Equation 12 with u^+ as a function of y^+ with different roughness values [33].

9 Making Sense of Unsteady Flow

Interpretation of unsteady flow can be difficult due to its complexity and large number of length scales and time scales. One of the advantages of unsteady simulation is that the velocity vectors and flow quantities are well defined spatially and temporally. This allows for advanced visualization approaches to be used to understand the flow. In the previous sections contour plots were presented and are used extensively. There are also other approaches to visualize the velocity field.

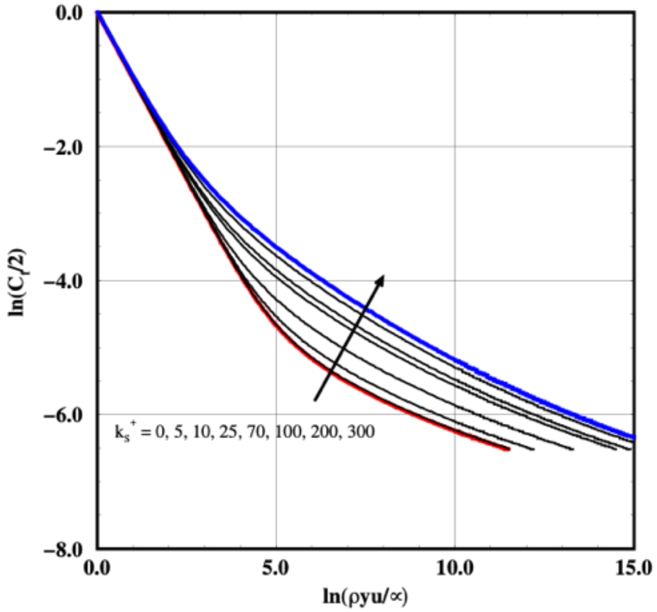

FIGURE 47: Plot of Equation 14 with C_f as a function of Re with different roughness values [33].

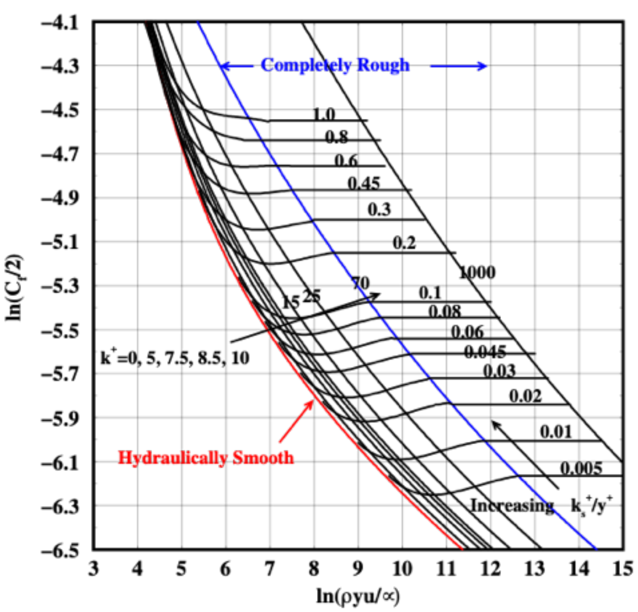

FIGURE 48: Plot of Equation 14 similar to Figure 47 but also showing lines of constant $\frac{k^+}{y^+}$ [33].

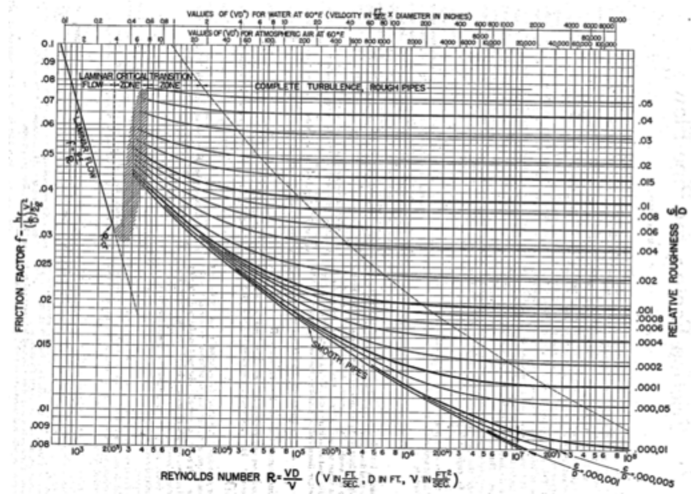

FIGURE 49: Moody diagram used to get the friction factor in smooth and rough pipes and ducts for turbulent flow (from the 1944 paper by Moody [35].

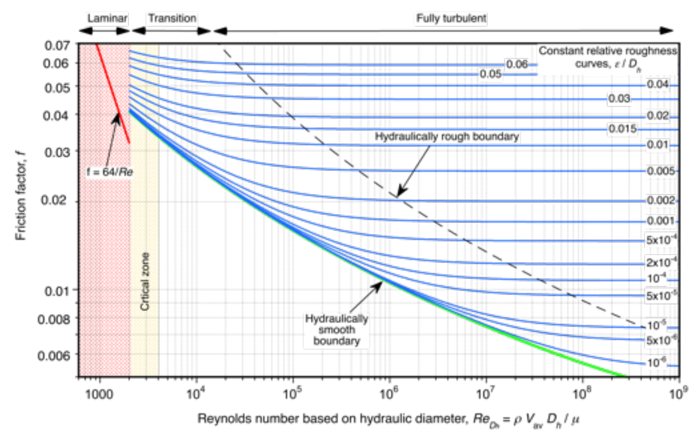

FIGURE 50: Easier to read Moody diagram used to get the friction factor in smooth and rough pipes and ducts for turbulent flow (figure from ref [38] which has a Creative Commons Attribution-NonCommercial-NoDerivatives 4.0 International License).

9.1 Streamlines, Pathlines, Streaklines

Anderson [39] defines pathlines, streamlines, and streaklines. To paraphrase these definitions,

> a pathline is the curve that follows the path of an infinitesimal small fluid element,
> a streamline is a curve that is everywhere tangent to the velocity vector at that point, and
> a streakline is the curve that traces the fluid elements going through a fixed point in space.

For steady flow, pathlines, streamlines, and streaklines are all the

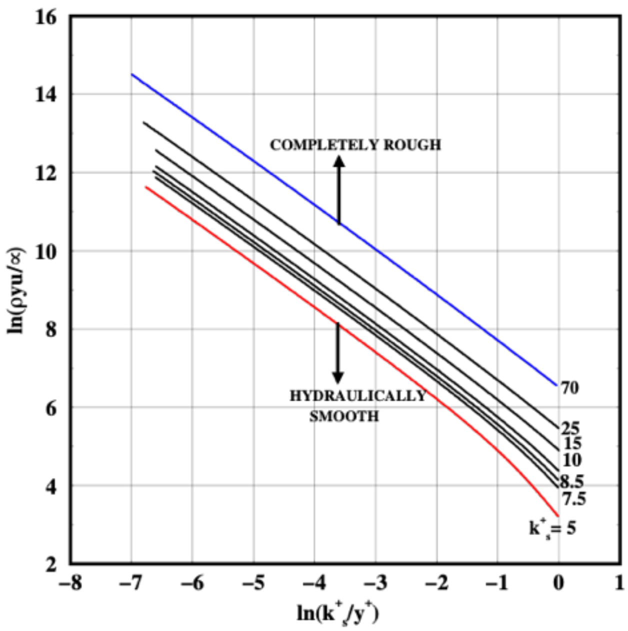

FIGURE 51: Re as a function of $\frac{k^+}{y^+}$ and k_s^+ used to get the value of $\frac{k^+}{y^+}$ [33].

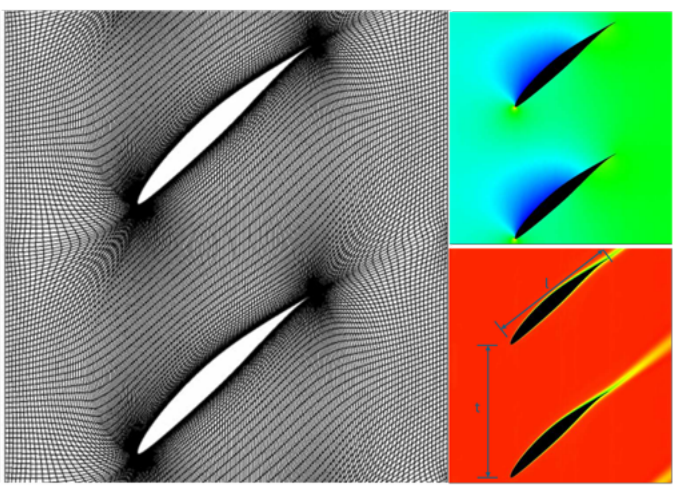

FIGURE 52: The grid (on left) and contours of static pressure (upper right) and total pressure (lower right). These contours are for the smooth case. Geometry parameters are shown on the total pressure contour [33].

same curves.

Three applications are shown in the next three subsections that use pathlines and streamlines and have relevant flow physics that are of interest.

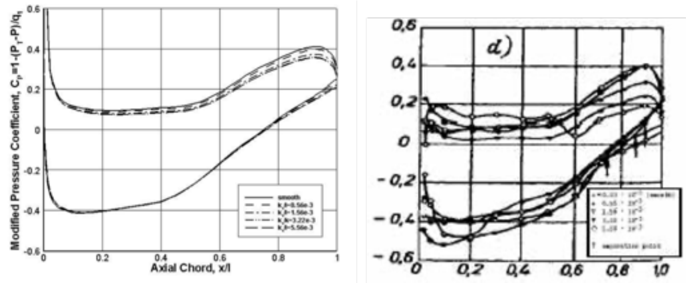

FIGURE 53: Pressure coefficient distribution for the five roughness values for the NACA 65-6 10 with a t/l=1.0. Re=4.3e5, M-0.11, inlet angle of 48 degrees. The plot at the left is from the simulation and at the right is from an experiment [36] [33].

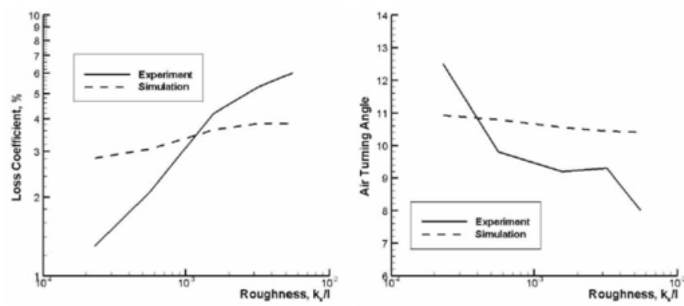

FIGURE 54: Loss coefficient (left) and air turning angle (right) evaluated at $t/4$ downstream of the trailing edge for the simulation and experiment for different values of roughness [36] [33].

9.2 Low Pressure Turbine with High Casing Wall Slope

The Low Pressure Turbine (LPT) for the EEE engine was designed and the testing allowed for many configurations in order to understand the effects of the different blade rows since it is not possible to instrument between the blade rows. The design had high wall slope at the casing in order to get increase the radius of the LPT as much as possible to get the wheel speed higher. The two-stage LPT configuration is shown in Figure 55. Experiments were run as vane-only, stage one, stage one plus the vane for stage 3, and the two-stage configuration as shown in the figure. Subsequent tests of a redesigned vane, a redesigned two-stage group and the complete 5-stage configuration of the full LPT were also run. The simulations that were run and described by me in a paper [40] are for the vane-only, the single stage, the single stage with vane two and the two-stage group. A summary of the setup and results of the vane-only and single stage follow.

The inlet total pressure profile was measured and the profile is shown in Figure 56. The boundary layer at the casing that takes up 5% of span near the casing is turned by the vane and is heavily influenced by the high endwall slope. The computation for the vane-only configuration utilized the Average Passage Code described in the previous section. Since this is only for the solution of one blade row, the Average Passage terms are not utilized. The experimental and computational total pressure contours are shown for a location downstream of the vane in Figure 57. The comparison is quite good. Although there is evidence of a vortex at the hub with low total pressure at the core of that vortex, the dominant feature is the low total pressure in a vortex core about 85% span where the 0.945 is shown in the experimental results (left) and 0.940 in the computational results. This feature is due to the roll up of the casing boundary layer into a strong vortex due to the turning of the vane by roughly 60°. Notice that the vortex is away from the casing at this station since the low total pressure in the vortex cannot follow the high slope at the casing.

The single stage configuration was run three ways. The first used the Average Passage Code for the two blade rows consisting of the vane and rotor. The second was as an unsteady simulation using the Turbo code [41] [42] for the rotor where the vane-only solution was used to generate the unsteady upstream boundary condition by converting the tangential variation of total pressure and swirl into the necessary time varying condition. The third approach was to run the rotor-only but with a profile of tangentially averaged total pressure and swirl.

Figure 58 compares the profile of stage efficiency which is evaluated from the Total Pressure and Total Temperature as described in the appendix of the EEE LPT report [43]. Notice the hole in efficiency from 50 to 85% span in the experimental data. The unsteady simulation captures a hole in efficiency although at a higher span. In the paper by Turner [40], it is speculated that the radial extent of this efficiency deficit might be because the shroud cavities and their flows were not modeled. The vortex at the vane trailing edge centered near 85% span appears to carry through the rotor to be the cause of the efficiency hole.

Figure 59 shows the pathlines that are generated by starting the particles at the same location in the rotor domain of reference at three different spans. At the lower span near the hub and the upper span near the casing, one can see how the flow can go to very different spanwise locations due to getting caught up in the vortices. This produces a lot of spanwise mixing which is an advection process and not a diffusion process.

♢ **Key Takeaway 7.** *High endwall slope of the casing of a low pressure turbine vane can be used to increase the radius and raise the rotation velocity. However this high slope means that low momentum fluid may not stay attached to the endwall. It then appears to be a deficit in total pressure at a lower span.*

9.3 Stage Matching Investigation (SMI)

The Compressor Aero Research Lab (CARL) facility at the Air Force Research Lab (AFRL) is used to experimentally investigate high speed compressor flow physics, and is also a very useful facility for validation of computational tools. There was an interest in the effect of blade row gap on performance so a series of tests called Stage Matching Investigation (SMI) took place. The SMI rig had a Wake Generator (WG), rotor, and stator, although the configuration chosen for numerical comparisons in a papers by Turner et al [44] [45] were the WG-rotor configuration shown in Figure 60. Three spacings were explored in the experiment whereas only the close and far locations are presented in the journal paper and are shown in Figure 61. The WG design was explained by Chris et al. [46], Gorrell [47], and Gorrell et

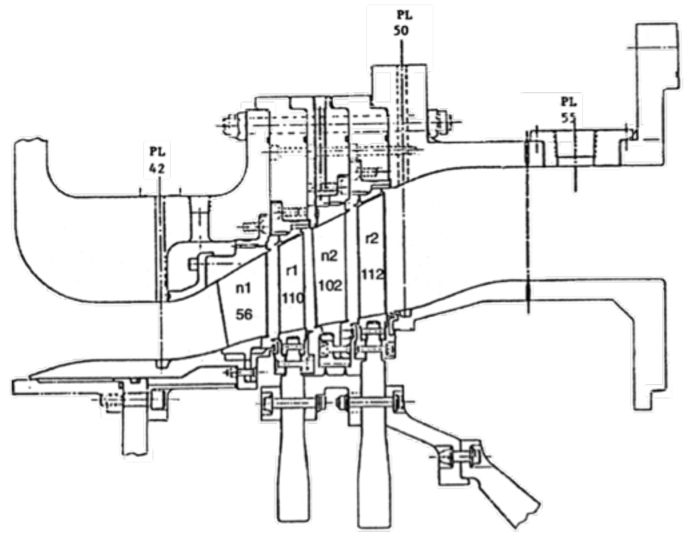

FIGURE 55: EEE two-stage Low Pressure Turbine rig (configuration 4) [40] [43].

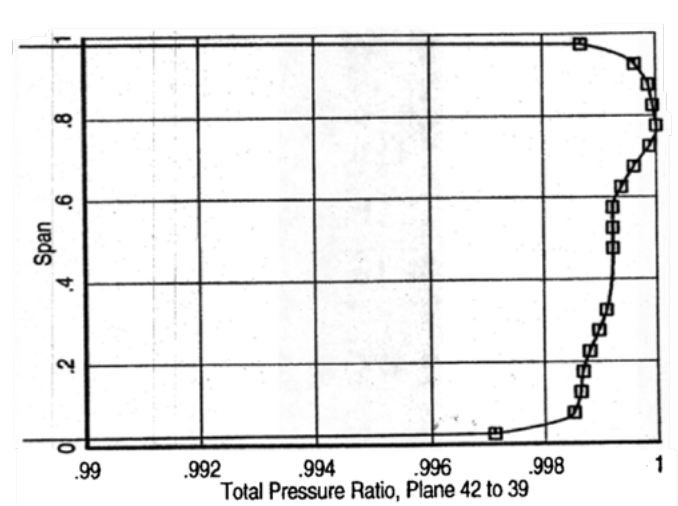

FIGURE 56: Experimental total pressure profile at the inlet plane used in the vane-only simulation [40].

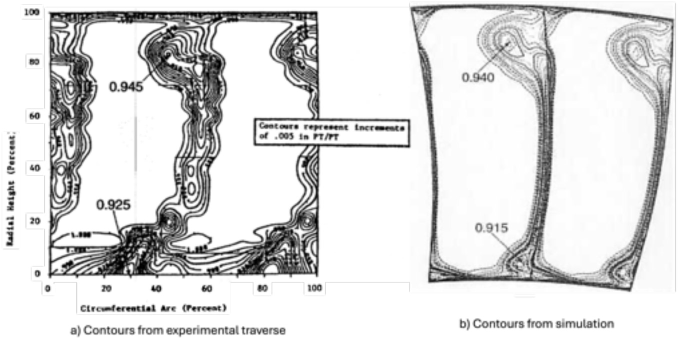

FIGURE 57: Contours of total pressure just downstream of the first vane trailing edge for the vane-only configuration. Contour plot intervals are the same for each plot. [43] [40].

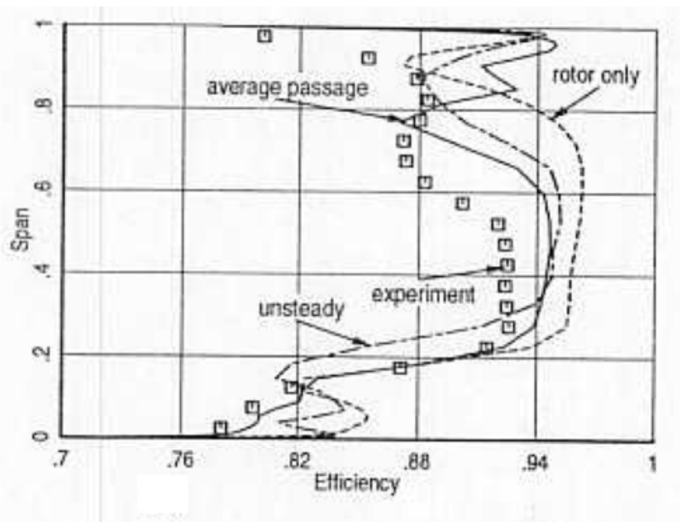

FIGURE 58: Comparison of the total-to-total stage efficiency profiles downstream of rotor 1 for the single stage (vane-rotor) configuration. The efficiency is evaluated from the measured and simulated total pressure and total temperature profiles. [40].

al. [48]. The WG are uncambered symmetric airfoils with small leading edge and thick trailing edge as shown in Figure 62 along with the computational grid details. The WG creates a large base drag and no swirl. Solidity is held constant from hub to tip by varying the chord in order to keep the spanwise loss and wake width nearly uniform.

The CFD approach used APNASA and Turbo, the same codes used for the application in the previous subsection. However, the generalized closure of the average passage terms allowing for non-uniform H-grids was used as described by Kirtley et al. [21]. There are 24 wake generator blades and 33 rotor blades.The grid resolution used is shown in Figure 62. and the

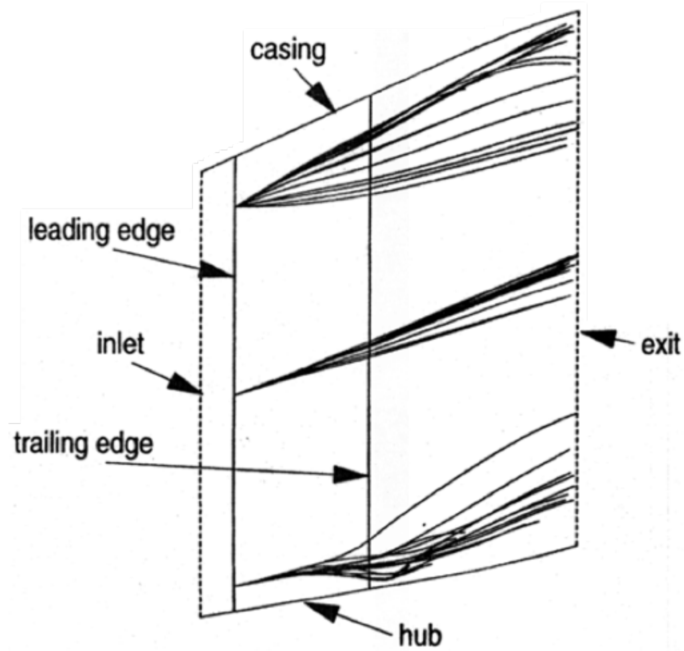

FIGURE 59: Meridional view of the pathlines in rotor 1 from the unsteady rotor 1 simulation. The pathlines have been started from the center of the passage at the leading edge plane at three spanwise locations. [40].

APG grid generator developed by Tim Beach [49] was used.

Figure 63 shows the comparison of the experimental and computational Total Pressure and Total Temperature profiles at the travers plane for the close and far configurations. The efficiency profiles comparison is shown in Figure 64, and Figure 65 shows the difference in efficiency (far minus close) for the experiment and computations. Table 1 shows the one dimensional difference (far minus close) in efficiency. From the one dimensional comparison, it appears that the APNASA simulation does a better job matching the experiment. However, the profiles in Figure 65 show that Turbo is matching better, but that the absense of data near midspan, the experimental value of the difference would be lower. This leads to a takeaway.

◇ **Key Takeaway 8.** *Good experiments and good computations will complement each other to gain more understanding than either approach alone. Also, one must be careful when comparing high-level one-dimensional numbers between experiments and simulations. Both have finite resolution and that resolution must be taken into account.*

For the close configuration at an instant in time (3/4 period) the unsteady Turbo simulation blade-to-blade contours of entropy, radial velocity and radial vorticity are shown in Figure 66 for 65% and 90% span. The thick trailing edge of the WG pro-

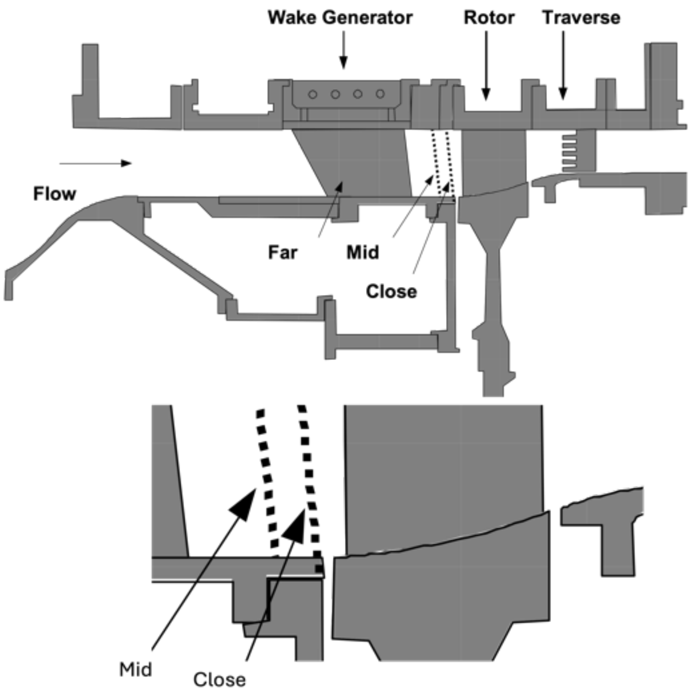

FIGURE 60: SMI geometry for two blade row configurations (no stator) [45]. The far and close configurations were explored in detail computationally.

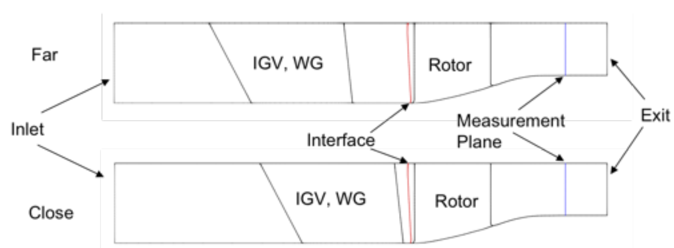

FIGURE 61: Grid domain for the far and close configuration simulations [45].

	Efficiency Difference (%)
Experiment	0.445
Turbo	1.008
APNASA	0.461

TABLE 1: One dimensional comparison of the efficiency difference between far and close.

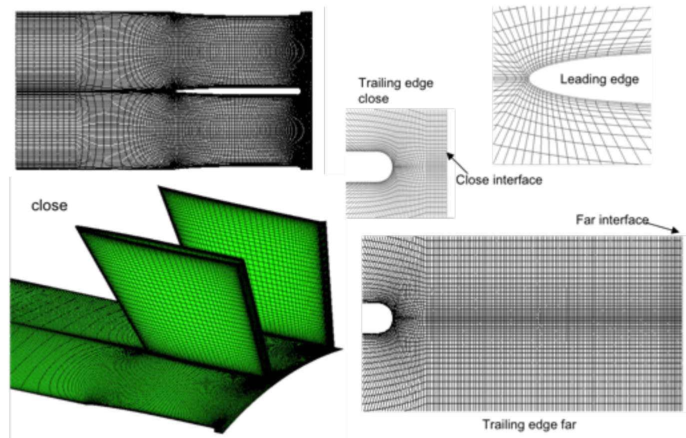

FIGURE 62: Wake Generator (WG) with detail at the leading and trailing edges (close is 61x71x138 in the blade-to-blade, radial, and axial directions. LE is 21, TE is 111, and the number of blades is 24). Spanwise location of the 3D sections shown are at j=36 or 71.6% span [45].

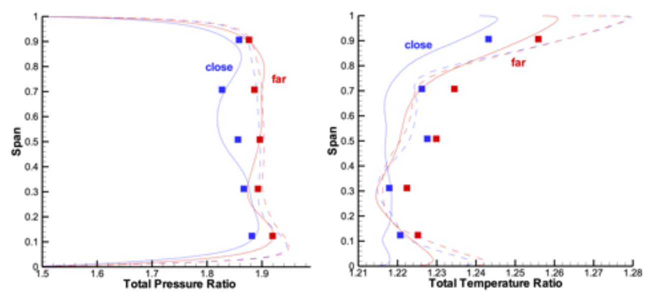

FIGURE 63: Total Pressure and Total Temperature profile comparisons between experiment, APNASA and Turbo simulations for both the close and far configurations [45].

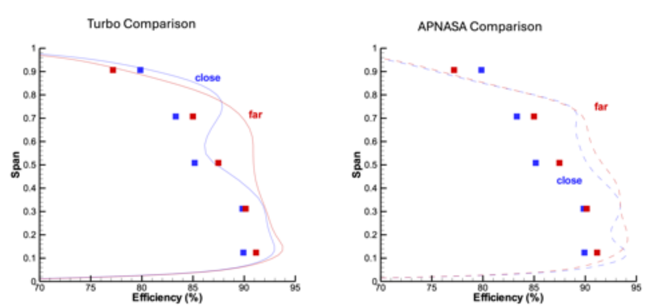

FIGURE 64: The efficiency profiles comparing the unsteady Turbo (left plot) and APNASA (right plot) simulations with experiment at the close and far configurations [45].

structive to follow the trajectory of the tip vortex in a transonic compressor rotor, especially at different operating conditions.

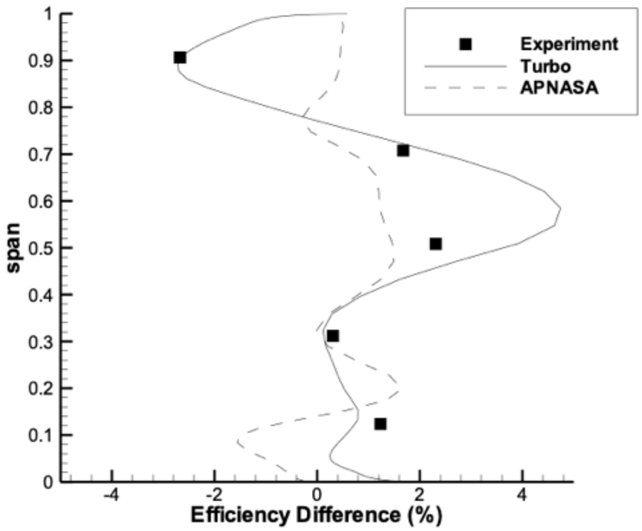

FIGURE 65: Profiles of efficiency difference between far and close configurations for the Turbo and APNASA simulations and the experiment [45].

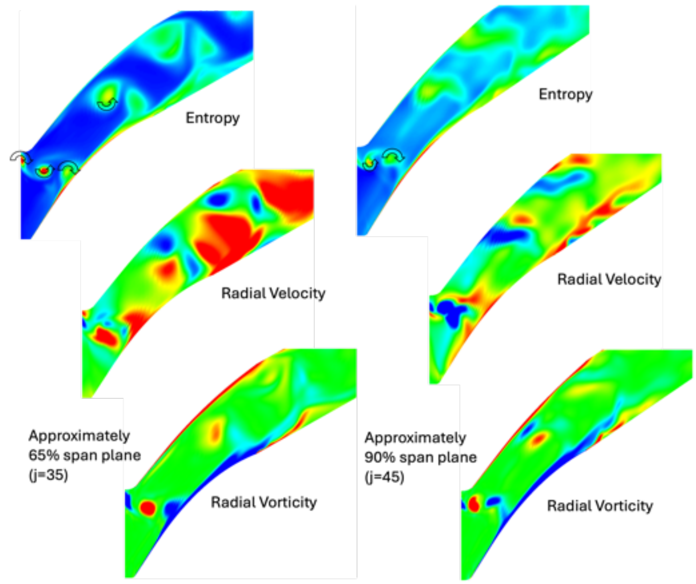

FIGURE 66: Blade-to-blade contours of an instantaneous rotor solution (time=3/4 period) from the Turbo solution in the close configuration at 65% and 90% span [45].

duces a shed vortex up and down the span that is phase-locked with the rotor passing which produces and unsteady lift on the WG due to the rotor bow shock going by in time. The entropy contour show the direction of rotation of this shed vortex that is clearly seen in the radial vorticity contour, and can also be seen in the corresponding entropy plot. Figure 67 shows a view of the rotor blade forward looking aft that has an isosurface of radial vorticity with the radial velocity contours mapped onto that isosurface. The dominant shed vortex feature is the vortex in in Figure 66 that has a counter-clockwise arrow in the entropy plots. At 65% span the radial velocity is positive while it is negative at 90%span. Being able to visualize this shed vortex in 3D allows for a lot more understanding about its structure. The variations in radial velocity are indicative of the likelihood of spanwise mixing. This is shown by the pathlines in Figure 68 that all start at the same point in the rotor relative frame mid-rotor passage just upstream of the rotor leading edge. Some pathlines go as low as 50% span showing the huge extect the flow can get mixed out. The WG had an extremely thick trailing edge so the shed vortex is larger than a typical compressor trailing edge. However, it was useful to accentuate the flow physics. The BRI (Blade Row Interaction) test campaign that followed SMI allowed for a more realistic compressor stator geometry as reported by List [50] and List et al. [51].

Another obvious feature shown in Figure 67 is the leading edge tip vortex. The radial component of vorticity is only a part of the vorticity of this tip vortex. However it is often very instructive to follow the trajectory of the tip vortex in a transonic compressor rotor, especially at different operating conditions.

9.4 Hub Cavity Flows

In a compressor, a hub of a stator can either be cantilevered or shrouded as shown in Figure 69. For the cantilevered stator, there is a gap between the stator and rotating hub, whereas with the shrouded stator, there is a ring supporting all the stators around the annulus and a small gap between that ring and the rotating hub. Typically there is honeycomb or an abradable material on the inner part of the ring and 2 or 3 seal teeth on the rotating hub. Since the hub is spinning, power from the shaft will turn to heat due to a shear work which is the hub velocity times the shear force (the shear stress times the area). For the cantilevered stator, the gap is similar to a tip gap in a rotor. The shrouded stator is often considered to produce less loss since the clearance gap can typically be smaller. Mahmood [52] and Mahmood and Turner [53] explored details of the flow in a 3-blade row configuration (rotor-stator-rotor) with an emphasis on the hub clearance and hub cavities. A schematic of this is shown in Figure 70. The geometry was based on rotor 6, stator 6 and rotor 7 of the 10-stage EEE high pressure compressor with geometry from the geometry generator T-Blade3 (see subsection 13.1) and conditions defined in the EEE HPC report [54] [52]. Also explored in this study were different clearances by changing the inner radius of the shroud ring as shown in Figure 71.

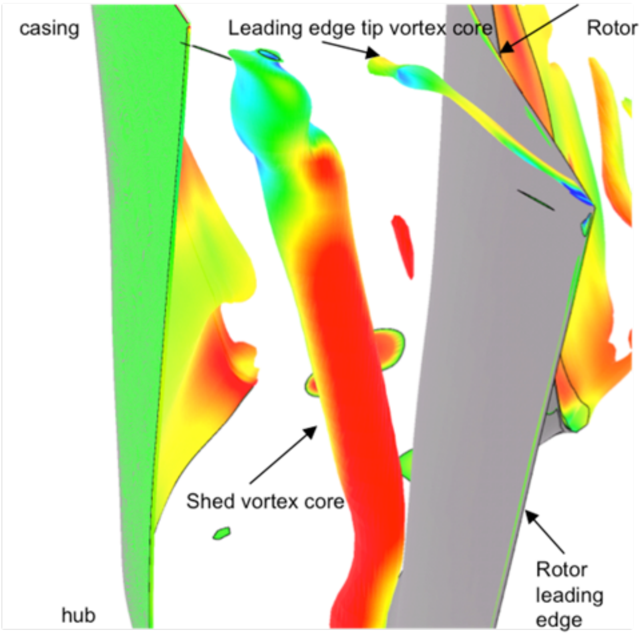

FIGURE 67: Radial velocity contours on a Radial Vorticity isosurfact of the t=3/4 rotor solution in the close configuration. Clearly seen are the shed vortex and tip vortex. The radial velocities are negative in the vortex near the tip. View is forward looking aft down midpassage [45].

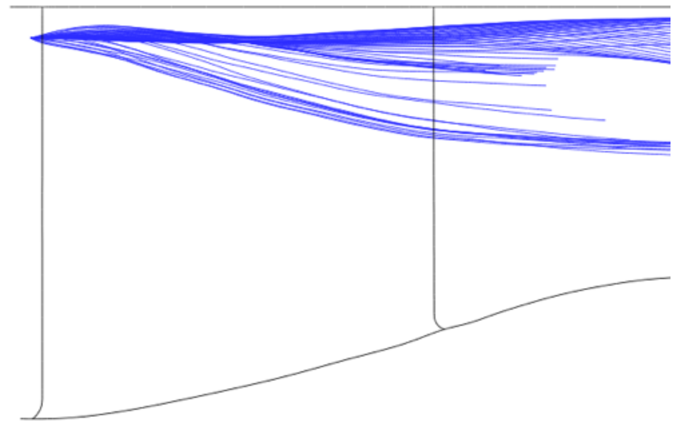

FIGURE 68: Axisymmetric projection of the particle paths (pathlines) in the rotor for the Turbo simulation of the close configuration. Particles were released near the tip just upstream of the leading edge and in the path of the pressure side shed vortex. A total of 55 solution files were used for one WG wake passing period representing every fourth time step. Some of the particles do not appear to go all the way downstream. Those left the domain of the single rotor passage [45].

The CFD solver FineTurbo along with the mesh generator, Autogrid and post processor CFVIEW were used for these simulations. These codes were developed by Numeca, but now are distributed and further developed by Cadence. Vilmin at al. [55] describes the implementation of the NonLinear Harmonic (NLH) approach for simulating unsteady flows. The 3-blade row simulations including cavities and seal teeth used the mixing plane approach as well the NLH method. Four different clearances were explored. Details of the CFD approaches are shown in both references mentioned [52] [53].

The sensitivity to clearance is shown in Figure 72 on the leakage across the cavities and seal teeth as well as the drop in efficiency with no cavity and leakage. The simulation results are shown in the bottom two plots. A series of experiments varying the hub clearance in a 4-stage low speed axial compressor was conducted by Wellborn [56]. The sensitivity at two loading conditions, peak efficiency and higher loading are shown in the upper two plots. The mass flow leakage for the simulation of the 1.5 stage case is lower than measured in the low speed rig. The efficiency decrease is comparable and demonstrates that the simulation of ht hub cavity flows can realistically capture the losses.

Figure 73 shows the streamlines based on the axisymmetric average velocity field for four of the clearance values simulated. Figure 74 is just the clearance of 0.7% span case. The streamlines show the complicated flow field created in the cavities as well as the jet of fluid going upstream across the seal teeth.

Figure 75 shows the profiles of the static pressure at the stator trailing edge plane For the no-cavity case, the static pressure profile is nearly flat whereas there is a significant drop in the static pressure near the hub which is slightly more pronounced as the clearance increases. This drop in static pressure is due to the curvature of the flow as it enters into the cavity. Figure 76 shows the profile of entropy at the rotor leading edge plane showing an increase in entropy due to the leakage flow coming back into the main flow path.

♢ **Key Takeaway 9.** *Due to the static pressure change across a compressor stator, the flow goes through the seal teeth from downstream to upstream. Tighter clearances reduce the mass flow through the cavities and seal teeth. However the Total Temperature rise across the seal teeth will be grater for the tighter clearance.*

9.4.1 Shear Work Through the Cavity

A model for the leakage and shear work has been presented by Millwards and Edwards [57] [58] . A different model that uses the the wall functions with roughness that were derived from Spalding's formula in subsection 8.3 has been developed by Mahmood and

Turner [53]. The comparison of those models with the CFD is shown in Tables 2 and 3.

	0.5% span	0.75% span	0.9% span	1.3% span
Mass Averaged rise in absolute TT (K)	72.39	58.78	49.47	42.73
Leakage mass flow (kg/s)	0.13	0.19	0.27	0.36
Shear work done through the cavity (KW)	9.54	11.18	13.24	15.48

TABLE 2: Cavity and seal teeth one dimensional results for different clearances.

	CFD Results	Millward et al. Correlation	Mahmood model
Shear work done through the cavity (KW)	15.48	11.59	11.11
Leakage mass flow rate (kg/s)	0.36	0.36	0.36
Rise in Total Temperature (K)	42.73	32.00	30.68

TABLE 3: Comparison of CFD results at the 1.3% span clearance (C=0.45 mm) and two shear work models.

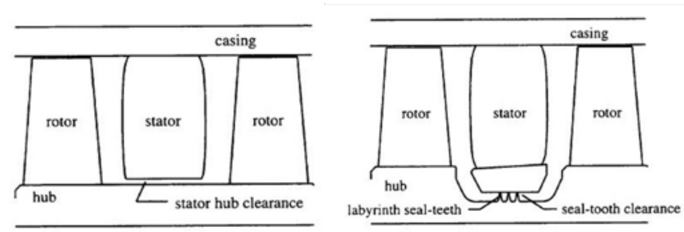

FIGURE 69: Schematics of a cantilevered stator (left) and a shrouded stator (right) [53].

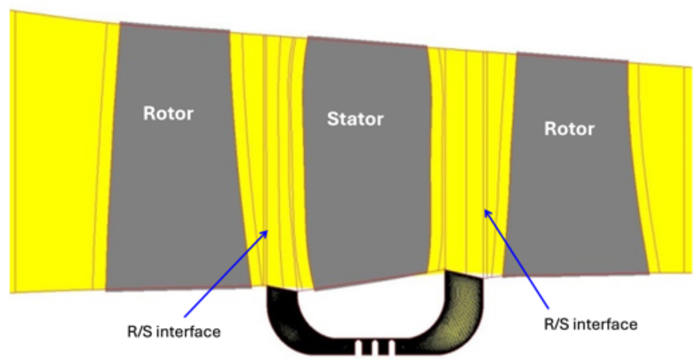

FIGURE 70: Computational domain showing the two rotors, the shrouded stator with the cavities, seal teeth and the rotor-stator interfaces [53].

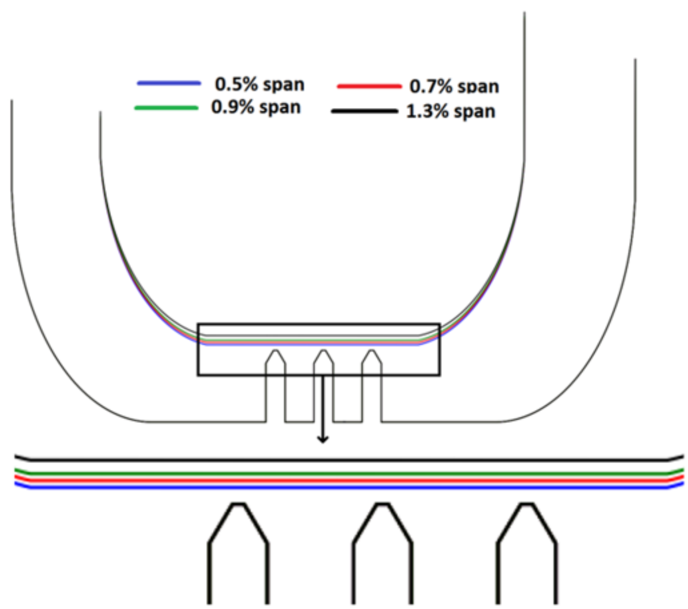

FIGURE 71: Detail of the stator cavity region showing how the clearance was varied for the clearance study [53].

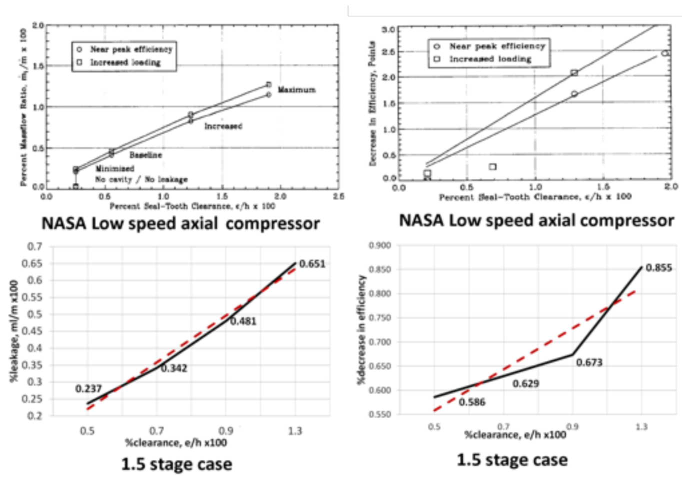

FIGURE 72: Experimental clearance sensitivity results from the NASA low speed axial compressor [56] (above) compares to the computational results for the 1.5 stage compressor [53] (below).

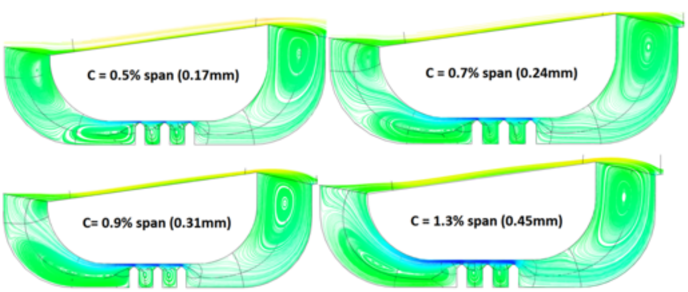

FIGURE 73: Streamlines in the cavity region for 4 different clearance values based on the tangential averaged velocities [53].

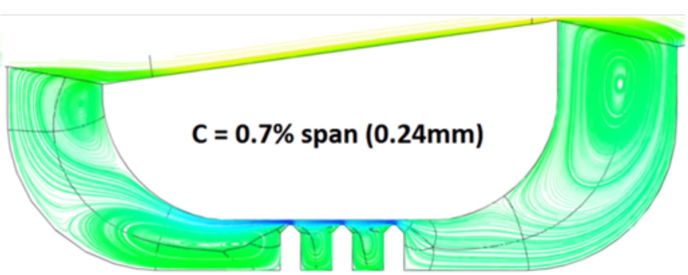

FIGURE 74: Streamlines in the cavity region for the 0.7% span clearance [53].

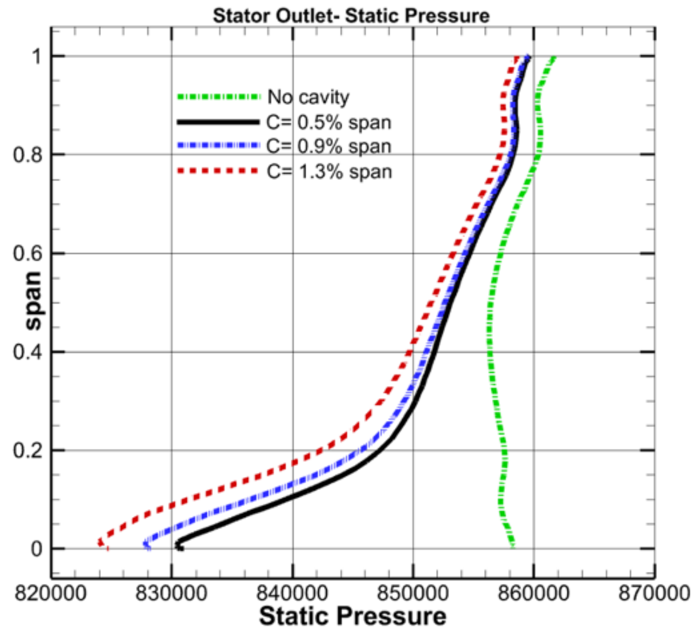

FIGURE 75: Tangentially averaged static pressure profile at the stator trailing edge plane [53].

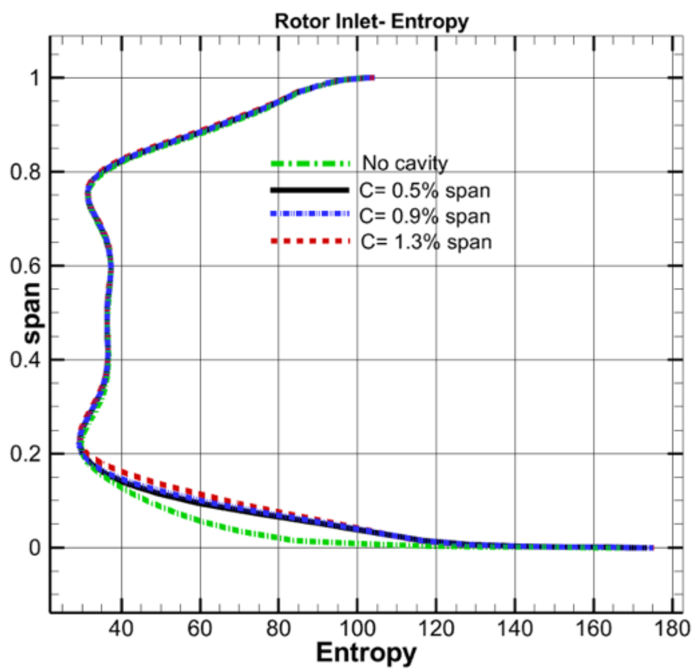

FIGURE 76: Tangentially average Entropy profile at the downstream rotor leading edge plane [53].

9.5 Relation to Turbulence

9.6 Large Eddy Simulation (LES)

9.7 Cooled Turbine

10 Heat Transfer in a Compressor

11 Biomickery and Simulation of a Maple Seed

12 The Role of Curvature in Turbomachinery Design

13 Optimization

Optimization exploits the simulation capabilities at the right fidelity to create improved designs.

13.1 Parametric Blade Geometry Generator, T-Blade3

13.2 2D Mises

13.3 3D

13.4 Supercritical CO_2 Compressor

13.5 Structures Optimization

13.6 Open Rotor Stage

14 CONCLUSIONS

This paper has presented simulation tools that I have either directly developed or collaborated on developing. These tools have been utilized in the design process to create better turbomachinery, much of which flies every day. The details and importance of the models has been articulated. Validation cases have been presented that demonstrate the comparison of the simulations with experiment that gives confidence these tools can be trusted in the design process.

15 Future of Simulations

15.1 Propulsion-Airframe Integration

16 ACKNOWLEDGEMENTS

There are hundreds of people to acknowledge and thank for giving me the knowledge, insights, and opportunities throughout my life and career. However there is not room to thank everyone. I specifically want to thank my wife, Nancy G. Turner, who has put up with my geekiness and not finishing sentences for 45 years. I want to acknowledge my two sons Luke and Graham, and their wives Reina Dickey and Tala Turner. My older brother Cary, who passed away 2 1/2 years ago, his wife Laurie, and my other living siblings, Amy, Jim and his wife Nancy, Nancy, and David and his wife Brenda. I want to acknowledge the impact my grandfather, Lucien McKee Grant, had, although he died when I was only 14 years old. He was an admiral in the US Navy, an early Naval Aviator, in the first class of Aeronautical Engineers in the US government and was an active member of the NACA. I want to thank and acknowledge the help Paul Giel has given with this paper, and the following people who have had a huge impact on my career: James (Jim) Keith, Leroy (Roy) Smith, Mike Suo, Mike Giles, Mark Drela, Steve Almaras, Ian Jennions, John Adamczyk, Tony Strazisar, Paul Orkwis, Ken Suder, D.R. Reddy, Mark Celestina, and Brian Forbes. I want to acknowledge the hundreds of students I've worked with as a professor. I learn more from them than I teach. Thanks also go to my coach, Brian Forbes. I have a spreadsheet that I compiled that includes names from high school, Virginal Tech, UC, MIT, GE, ETH, NASA, ASME, AFRL, NPS, and other people I have known. It includes over xxx names.

Thank you to the ASME IGTI Honors and Awards Committee who selected me to be the scholar lecturer and especially the chair, Doug Nagy, who has done a great job of having me keep to the schedule and getting reviewers who I also thank. I also want to thank the NASA Glenn Research Center and the people there who have helped support this paper.

REFERENCES

[1] Judy Conlin. Striving for peak design. In *InSights, NASA High Performance Computing and Communications*, volume 2, pages 2–7. NASA, 1997.

[2] JOHN D. DENTON. Some limitations of turbomachinery cfd. In *ASME GT2010-22540*, Glasgow, UK, 2010.

[3] M. G. Turner and J. S. Keith. An implicit algorithm for solving 2d rotational flow in an aircraft engine fan frame. Number AIAA-85-40965. AIAA, 1985.

[4] M.D. Bowles. *The "Apollo" of Aeronautics, NASA's Aircraft Energy Efficiency Program 1973-1987*. NASA, www.nasa.gov/pdf/601247main_apolloaeronautics-ebook.pdf edition, 2010.

[5] T.J. Sullivan, G.W. Luebering, and R.D. Gravitt. Energy efficient engine, fan test hardware detailed design report. NASA Report Number CR-165148, GE Aircraft Engines and NASA, October 1980.

[6] H.-W. D. Chiang and M.G. Turner. Compressor blade forced response due to downstream vane-strut potential interaction. *Journal of Turbomachinery*, 118(1):134–142, January 1996.

[7] Mark G. Turner. Aegis user's manual. Technical Memorandum 84-AEG-1154, GE Aircraft Engines, 1985.

[8] D.G. Holmes and S.S. Tong. A three-dimensional euler solver for turbomachinery blade rows. *ASME Journal of Turbomachinery*, 107:258–264, 1985.

[9] B. S. Baldwin and H. Lomax. Thin layer approximation and algebraic model for separated turbulent flows. Number AIAA 78-257. AIAA, 1978.

[10] B. E. Launder and D. B. Spalding. The numerical computation of turbulent flows. *Computer Methods in Applied Mechanics and Engineering*, pages 269–289, 1974.

[11] Chen Y. S. Compuation of turbulent flows using an extended k-ε turbulence closure model. Technical Report NASA-CR-179204, NASA, 1987.

[12] M. G. Turner and I. K. Jennions. An investigation of turbulence modeling in transonic fans including a novel implementation of an implicit $k-\varepsilon$ turbulence model. *ASME Journal of Turbomachinery*, 115:249–260, 1993.

[13] I. K. Jennions and M. G. Turner. 3-d navier-stokes computations of transonic fan flow using an explicit flow solver and an implicit $k-\varepsilon$ turbulence model. *ASME Journal of Turbomachinery*, 115:261–272, 1993.

[14] J. D. Denton. Loss Mechanisms in Turbomachines. *ASME Journal of Turbomachinery*, 115(4):621–656, 1993.

[15] Mark G. Turner, Te Liang, Phillip P. Beauchamp, and Ian K. Jennions. The use of orthogonal grids in turbine cfd computations. Number ASME 93-GT-38, 1993.

[16] J. J. Adamczyk. Model equation for simulating flows in multistage turbomachines. ASME Paper 85-GT-226, 1985.

[17] J. J. Adamczyk. Aerodynamic Analysis of Multistage Turbomachinery Flows in Support of Aerodynamic Design.

ASME Journal of Turbomachinery, 122(2):189–217, 2000.

[18] J. J. Adamczyk, M. L. Celestina, T. A. Beach, and M. Barnett. Simulation of 3-dimensional viscous flow within a multistage turbine. *Journal of Turbomachinery*, 112(3):370–376, July 1990.

[19] I. K. Jennions and J. J. Adamczyk. "Evaluation of the Interaction Losses in a Transonic Turbine HP Rotor/ LP Vane Configuration". ASME Paper 95-GT-299, 1995.

[20] Mark L. Celestina and Richard A. Mulac. Assessment of stage 35 with apnasa. Number AIAA 2009-1057. AIAA, January 2009.

[21] K. R. Kirtley, M. G. Turner, and S. Saeidi. An average passage closure model for general meshes. 1999. ASME Paper 99-GT-077.

[22] J.K. Dukowicz. Conservative rezoning (remapping) for general quadrilateral meshes. *J. Comp. Phys.*, 54:441–424, 1984.

[23] D.E. Halstead, D.C. Wisler, T.H. Okiishi, G.J. Walker, H.P. Hodson, and H. Shin. Boundary layer development in axial compressors and turbines part 1 of 4: Composite picture. *Journal of Turbomachinery*, 119:114–127, 1997.

[24] S.D. Hunter. *Source Term Modeling of Endwall Cavity Effects on Gaspath Aerodynamics in an Axial Flow Turbine*. PhD thesis, University of Cincinnati, November 1998.

[25] Robert V. Garvin. *Starting Something BIG: The Commercial Emergence of GE Aircraft Engines*. AIAA, Reston, VA, 1998.

[26] N-S Liu. On the comprehensive modeling and simulation of combustion systems. Number AIAA Paper 2001-0805. AIAA, Jan 2001.

[27] M.G. Turner, Paul H. Vitt, David A. Topp, Sohrab Saeidi, Scott D. Hunter, Lyle D. Dailey, and Timothy A. Beach. Multistage simulation of the ge90 turbine. Number ASME 99-GT-98. ASME, 1999.

[28] M.G. Turner. Full 3d analysis of the ge90 turbofan primary flowpath. Technical report, General Electric Company, NASA-CR-2000-209951, March 2000.

[29] M.G. Turner, Rob Ryder, Andrew Norris, Mark Celestina, Jeff Moder, Nan-Suey Liu, John Adamczyk, and Joe Veres. High fidelity 3d turbofan engine simulation with emphasis on turbomachinery-combustor coupling. Number AIAA 3003-3769 in July. AIAA, 2002.

[30] Mark G. Turner, Andrew Norris, and Joseph Veres. High fidelity 3d simulation of the ge90. Number AIAA-2003-3996. AIAA, 2003.

[31] Mark G. Turner, John A. Reed, Robert Ryder, and Joseph P. Veres. Multi-fidelity simulation of a turbofan engine with results zoomed into mini-maps for a zero-d cycle simulation. Number ASME GT2004-53956. ASME, 2004.

[32] Mark G. Turner. Lessons learned from the ge90 3d full engine simulations. Number AIAA-2010-1606. AIAA, 2010.

[33] Aamir Shabbir and Mark G. Turner. A wall function for calculating the skin friction with surface roughness. Number GT2004-53909. ASME, 2004.

[34] H. Schlichting. *Boundary Layer Theory*. McGraw Hill, 1955.

[35] L.F. Moody. Friction factors for pipe flow. *Transactions of the ASME*, 66(8):671–684, 1944.

[36] K. Bammert and R. Milsch. Boundary layers on rough compressor blades. Number 72-GT-48, San Francisco, CA, March 1972. ASME.

[37] Karl Bammert and Reinhold Milsch. Das verhalten der grenzschichten an rauhen verdichterschaufeln. *Forschung im Ingenieurwesen*, 38(4), 1972.

[38] J. Gordon Leishman. *Introduction to Aerospace Flight Vehicles*. Embry-Riddle Aeronautical University, Creative Commons Attribution-NonCommercial, 2023.

[39] John D. Anderson. *Fundamentals of Aerodynamics*. McGraw Hill, New York, 5th edition, 2011.

[40] M.G. Turner. Multistage turbine simulations with vortex-blade interaction. *Journal of Turbomachinery*, 118(4):643–653, October 1996.

[41] J. P. Chen and D. L. Whitfield. Navier-Stokes Calculations for the Unsteady Flowfield of Turbomachinery. January 1993. AIAA Paper no. 1993-0676.

[42] Jenping Chen, M. L. Celestina, and J. J. Adamczyk. A new procedure for simulating unsteady flows through turbomachinery blade passages. In *ASME Turbo Expo 1994*, 1994. ASME Paper no. 94-GT-151.

[43] M.J. Bridgeman, D.G. Cherry, and J. Podersen. Nasa/ge energy efficient engine low pressure turbine scaled test vehicle performance report. Technical Report CR-168290, NASA, 1983.

[44] Mark G. Turner, Steven E. Gorrell, and David Car. A model of compressor blade row interaction with shock induced vortex shedding. In *42th AIAA/ASME/SAE/ASEE Joint Propulsion Conference & Exhibit*, 2006. AIAA Paper no. 2006-4459.

[45] Mark G. Turner, Steven E. Gorrell, and David Car. Radial migration of shed vortices in a transonic rotor following a wake generator: A comparison between time accurate and average passage approaches. *Journal of Turbomachinery*, 133:031018–1–031018–9, July 2011.

[46] R. M. Chriss, W. W. Copenhaver, and S. E. Gorrell. The Effects of Blade-Row Spacing on the Flow Capacity of a Transonic Rotor. *ASME Paper 99-GT-209*, 1999.

[47] Steven Ernest Gorrell. *An Experimental and Numerical Investigation of Stator-Rotor Interactions in a Transonic Compressor*. PhD thesis, Iowa State University, Ames, Iowa, 2001. Mechanical Engineering.

[48] S. E Gorrell, T. H. Okiishi, and W. W. Copenhaver. Stator-Rotor Interactions in a Transonic Compressor, Part 1: Effect of Blade-Row Spacing on Performance. *ASME Journal of Turbomachinery*, 125:328–335, 2003.

[49] Michael A. Kamp, Jason Nimersheim, Tim Beach, and Mark G. Turner. A turbomachinery gridding system. In *45th AIAA Aerospace Sciences Meeting and Exhibit*, 2007. AIAA Paper 2007-18.

[50] Michael G. List. Quarter annulus simulations of blade row interaction at several gaps and discussion of flow physics. Master's thesis, University of Cincinnati, Cincinnati, OH, August 2007.

[51] Michael G. List, Steven E. Gorrell, Mark G. Turner, and Jason A. Nimersheim. High fidelity modeling of blade row interaction in a transonic compressor. In *43rd AIAA/SAE/ASME Joint Propulsion Conference*, Cincinnati, OH, 2007. AIAA Paper no. 2007-5045.

[52] Syed Moez Hussain Mahmood. Optimization capabilities for axial compressor blade and seal teeth cavity. Master's thesis, University of Cincinnati, 2016.

[53] Syed Moez Hussain Mahmood and Mark G. Turner. Modeling capability for cavity flows in an axial compressor. In *ASME TurboExpo*, number GT2017-64040, Charlotte, NC, USA, June 2017. ASME.

[54] P.R Holloway, G.L. Knight, C.C. Koch, and S.J. Shaffer. Energy efficient engine high pressure compressor detail design report. Technical report, General Electric Company, NASA-CR-165558, 1982.

[55] S. Vilmin, E. Lorrain, C. Hirsch, and M. Swoboda. Unsteady flow modeling across the rotor/stator interface using the nonlinear harmonic method. Number GT2006-90210. ASME, 2006.

[56] Steven R. Wellborn and Theodore H. Okiishi. Effects of shrouded stator cavity flows on multistage axial compressor aerodynamic performance. Contractor Report 198536, NASA and Iowa State University, October 1996.

[57] J. A. Millward and M. F. Edwards. Windage heating of air passing through labyrinth seals. Number 94-GT-056. ASME, 1994.

[58] J. A. Millward and M. F. Edwards. Windage heating of air passing through labyrinth seals. *J. Turbomachinery*, 118(2):414–419, April 1996.

[59] Akshay B. Sudesh, Michael Boehler, and Mark G. Turner. Cfd simulation of flat plate film cooling of shaped hole using les,. In *AIAA Propulsion and Energy Forum and Exposition*, number AIAA 2019-4090. AIAA, August 2019.

[60] Akshay Sudesh. Cfd validation of flat plate cooling of cylindrical and shaped holes using rans and les computational models. Master's thesis, University of Cincinnati, January 2021.

[61] Michael Boehler, Akshay B. Sudesh, and Mark G. Turner. Hybrid eddy simulations of low reynolds number shaped hole film cooling on an adiabatic flat plate. In *AIAA Propulsion and Energy Forum and Exposition*, number AIAA 2019-4089. AIAA, August 2019.

[62] D. Bruna and M.G. Turner. A rothalpy analysis for the isothermal boundary condition at casing applied to the rotor 37 transonic axial flow compressor. Number GT2013-94595. ASME, June 2013.

[63] D. Bruna and M.G. Turner. Isothermal boundary condition at casing applied to the rotor 37 transonic axial flow compressor. *Journal of Turbomachinery*, 135(2013), May 2013.

[64] Mark G. Turner, Ahmed Nemnem, Anthony J. Gannon, Garth V. Hobson, and Wolfgang Sanz. Measured heat transfer in a transonic fan rig at casing with implications on performance. Number GT2015-43482. ASME, June 2015.

[65] Nicholas J. Georgiadis, Mark P. Wernet, Darrell S. Crowe, Carolyn Woeber, Kristen Karman-Shoemake, and Chad M. Winkler. *Summary of the 5¡sup¿th¡/sup¿Propulsion Aerodynamics Workshop Nozzle Test Case: Heated Nozzle Exhaust Passing Over A Film-Cooled Plate*. Number AIAA 2022-0086. AIAA, January 2022. URL: https://arc.aiaa.org/doi/abs/10.2514/6.2022-0086, arXiv:https://arc.aiaa.org/doi/pdf/10.2514/6.2022-0086, doi:10.2514/6.2022-0086.

[66] Mark G. Turner. The role of curvature in turbomachinery design. Number GPPS-2017-142. Global Power and Propulsion Society, 2917.